POLITECNICO DI MILANO

School of Industrial and Information Engineering

Master of Science in Mechanical Engineering

Quartz Crystal Microbalance: Temperature Effects Analysis

Advisor: prof. Bortolino Saggin

Co-advisor: prof. Diego Scaccabarozzi

Candidate:

Paolo Fileno RADDANI, 823087

Academic Year 2014-2015

To my Big Mama and my Moroccan Daddy

CONTENTS

INDEX OF FIGURES

INDEX OF TABLES

SOMMARIO

Lo studio riguarda gli effetti della temperatura su una microbilancia al quarzo per analisi termo-gravimetriche in applicazioni spaziali. La microbilancia oggetto di studio si differenzia da quelle comunemente discusse in letteratura per via dell'innovativo design di riscaldatore e sensore di temperatura, realizzati mediante film depositati direttamente sul cristallo. Per tale motivo, è atteso in fase di riscaldamento l'insorgere di un gradiente di temperatura, i cui effetti non sono stati ad oggi oggetto di ricerche approfondite.

Nella fase sperimentale dello studio, la misura di temperatura è stata effettuata mediante termografia all'infrarosso, mentre la modellazione ad elementi finiti è stata utilizzata per esaminare la resistenza meccanica e il comportamento dinamico della microbilancia. Un campo di temperature non uniforme è stato individuato sul cristallo per effetto della localizzazione della potenza termica fornita dal riscaldatore. Successivamente la deformata e gli sforzi derivanti sono stati calcolati mediante analisi ad elementi finiti.

Con lo stesso approccio è stato studiato il modo di vibrare di taglio. A temperatura, ambiente la frequenza propria è stata determinata correttamente a 10 MHz. Successivamente, un campo termico uniforme è stato applicato al cristallo al fine di ricavare la curva frequenza-temperatura. Lo stesso modello è stato testato a diverse temperature (fino a 90 °C) ed ha prodotto delle differenze con i valori sperimentali inferiori a 60 Hz. Successivamente, un gradiente di temperatura (90 °C al centro e 23 °C altrove) è stato applicato al modello. Da quest'ultima analisi è emersa una risonanza di 1.7 kHz più alta rispetto al caso con 90°C uniformemente distribuiti sul cristallo.

Si è dunque giunti alla conclusione che il design innovativo del riscaldatore è causa di un gradiente termico sul cristallo che, pur non essendo critico da un punto di vista della resistenza meccanica, provoca importanti variazioni di frequenza. Pertanto, al fine di ottenere risultati corretti dalle analisi termo-gravimetriche, sarà necessario compensare tali variazioni.

Parole chiave: *Microbilancia al quarzo, Oscillatore al cristallo, Termografia all'infrarosso*.

ABSTRACT

This study investigates the effects of temperature on the quartz crystal microbalance for thermogravimetric analyses in space. The studied microbalance differs from literature ones because of the device's innovative built-in heater and temperature sensor, made with deposited film over the crystal. Temperature gradient is expected on the crystal due to the presence of the built-in heater, an issue that has not yet been deeply investigated.

The crystal temperature was measured by means of infrared thermography, while a finite element approach served the purpose of investigating mechanical resistance and dynamic behavior. A non-uniform temperature distribution was detected when the heater circuit was fed, and thanks to the developed FE model, deformed shape and stress values were determined.

A dynamic model of the microbalance has been developed and the thickness shear frequency at ambient temperature was correctly found at 10 MHz. Uniform temperature distribution has been applied to the crystal in order to evaluate the frequency shift. The model was tested at temperatures up to 90 °C, providing differences with the experimental values smaller than 60 Hz. Moreover, a temperature gradient (90 °C at the center, 23°C at the edge of the disk) was applied in the model. The resulting resonance was 1.7 kHz higher with respect to the uniform 90 °C temperature field case, highlighting the importance of the temperature gradients on the microbalance performance.

The conclusion is that the microbalance's innovative heater causes thermal gradients that, although not critical from the point of view of mechanical resistance, ultimately cause frequency shifts. Thus, an experimentally determined correction factor for frequency will be necessary to correct the measurements during heating and retrieve correct results from thermogravimetric analyses.

Keywords: *Quartz Crystal Microbalance, Thickness Shear Mode Resonator, Infrared Thermography*.

CHAPTER 1

This chapter introduces the subject of the quartz crystal microbalances along with their possible space applications. It begins with motivating the need for such a device. Then, an overview of the theory is discussed, followed by basic information on the microbalance under study. Finally, the scope of the thesis is presented.

1.1 Introduction

The key of humans' understanding of many phenomena that happen in the solar system is the possibility of *in situ* measurements. Since the late 60s, the scientific community has put in a lot of work to develop sophisticated instruments to launch into space and to gather advanced data for scientists. For the latter, the problem of measuring very small masses is interesting in many different ways. Typical examples are the dust and water vapor detection in the Martian atmosphere (Battaglia, et al., 2004), the study of powders released by comets' nuclei (Srama, et al., 2011) or the general problem of contamination testing in space (McKeown, 1998). Quartz Crystal Microbalances are widely used for these scientifically critical purposes.

1.2 QCM: theory

The working principle of the Quartz Crystal Microbalance (QCM) is based on the piezoelectric property of quartz. Curie brothers first discovered piezoelectricity in 1880. They showed that charges appear on the crystal surface when loaded with a weight; the magnitude of the charges is proportional to the load (Curie & Curie, 1880). In 1881, Gabriel Lippmann mathematically predicted the converse piezoelectric effect: a voltage applied to the crystal surfaces induces a strain inside the material (Lippmann, 1881). Thus, a full coupling between mechanical and electrical properties of quartz is possible (Figure 1-1).

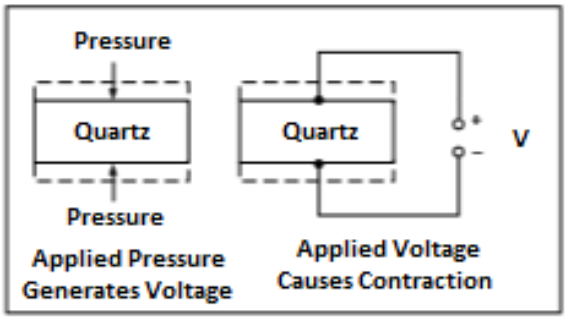

Figure 1-1. Piezoelectric effect.

Moreover, piezoelectricity is a linear effect: a reversal of the electric field reverses the strain, i.e., the mechanical deformations (Tiersten, 1969).

The nature of the piezoelectric effect is closely related to the anisotropic behavior of the crystal. A force that sufficiently deforms the lattice causes a net movement of positive and negative charges, which ultimately results in the manifestation of an electric dipole moment. Consequently, the centers of gravity of the positive and negative charges are distinct, and a voltage appears[1]. Nonetheless, this does not happen when the crystal has a perfectly isotropic lattice.
Piezoelectricity happens also when quartz interacts with an oscillating electric field. In this case, strains are oscillating too (Tiersten, 1969). For this reason, an elastic wave propagates through the material and it is known that the latter meets minimum impedance when the thickness of the device is a multiple of a half of its wavelength (O'Sullivan & Guilbault, 1999).

The QCM is a thickness shear mode (TSM) device in which the elastic wave propagates in a direction perpendicular to the crystal surface[2].
Pure thickness shear vibrations happen when the top and bottom surfaces slide parallel to each other for the same distance but opposite direction. This causes the midplane not to move at all and the lateral surface to deform in a shape similar to that shown in Figure 1-2.

[1] For example, a 1-cm^3 cube of quartz with 2 kN of correctly applied force can produce a voltage of around 12500 V (Repas, 2008).
[2] The velocities such waves in solids are typically close to 3,000 m/s (~10^{-5} times the velocity of light).

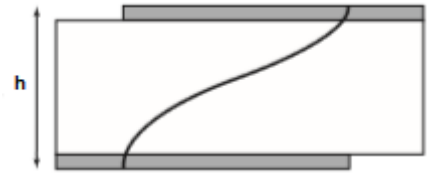

Figure 1-2. Lateral surface deformed shape.

Since quartz crystals show different modes of vibration depending on the orientation of the lattice (Figure 1-3), a precisely cut disk from a slab should be used in order to guarantee that thickness shear mode is possible.

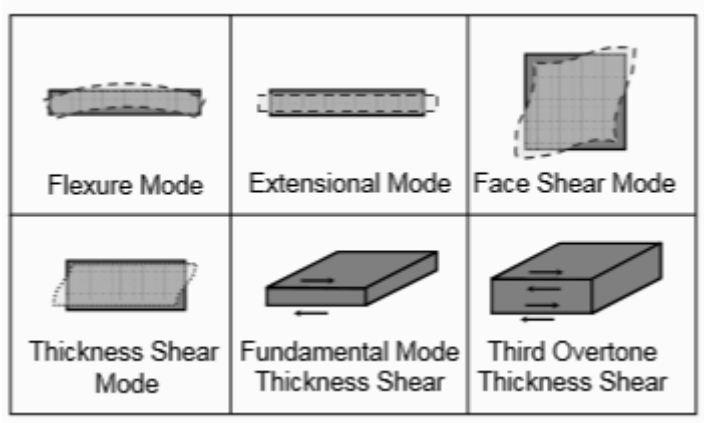

Figure 1-3. Possible vibration modes.

Figure 1-4 shows examples of cut planes for quartz crystal slabs. Among these, the *AT* cut is the most common choice for microbalance applications. The figure also defines the so-called *optical axes* (X, Y, and Z) that are referred to the quartz crystal and are different from the *local axes*, which are defined on the cut plane. This concept is very important since the physical properties of quartz listed in literature are generally referred to the crystallographic axes (Ward, 1992). This means that a change of coordinates is necessary to get values that are coherent with the cut under study. More details on this crucial topic will be provided in section 1.3.

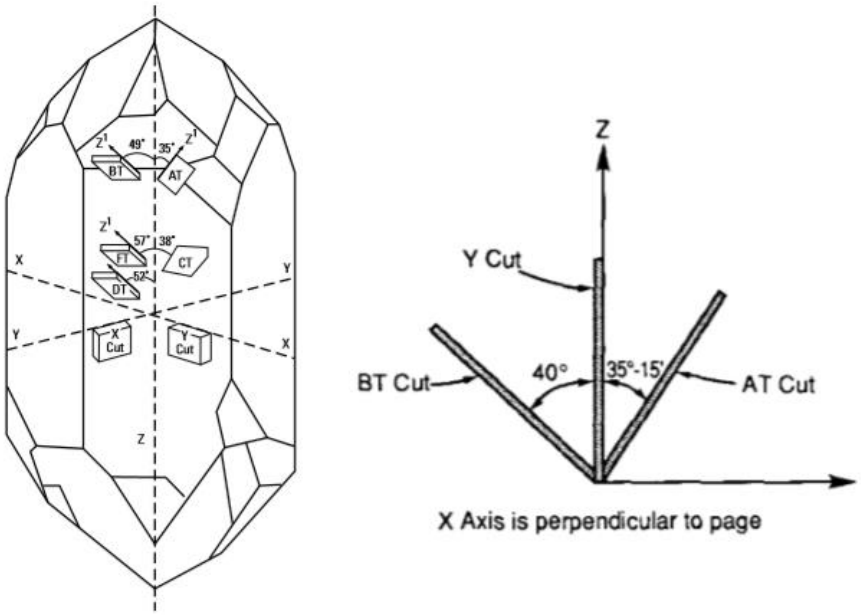

Figure 1-4. Typical cut planes for quartz crystals.

TSM is possible in an AT-cut quartz disk. The modal frequency can be analytically predicted. It was previously anticipated that the elastic waves tend to appear spontaneously when the thickness of the device is a multiple of a half of its wavelength. A simple consideration on wave propagation leads to the following equation.

$$f_n = \frac{v}{2h} \tag{1.1}$$

where v is the velocity of elastic wave (see note 2) and h is the thickness of the crystal. It is also known from the theory of modal analysis that

$$v = \sqrt{\frac{C_{ij}}{\rho}} \tag{1.2}$$

where ρ is the density and C_{ij} is the elastic modulus associated with the elastic wave being propagated[3]. By combining Eq. 1.1 and 1.2, it follows that

$$f_n = \frac{1}{2h}\sqrt{\frac{C_{ij}}{\rho}} \tag{1.3}$$

[3] The necessity of specifying the subscript *ij* will be clear when the anisotropic behavior of quartz will be discussed (section 1.3).

that is a simple expression for the vibration natural frequency. It is clear that the proper shear modulus must be used in Eq. 1.3 in order to study the TSM of quartz plates.
Experimental studies have produced an alternative equation to estimate the thickness shear frequency of a resonator, that is

$$N = f_n\, h \tag{1.4}$$

where f_n is the natural frequency, h is the thickness and N is a constant given for different cuts[4].
TSM happens also at odd multiples of f_n. These modes are called *overtones* and they are exploited when a high frequency resonator is needed (Figure 1-3).

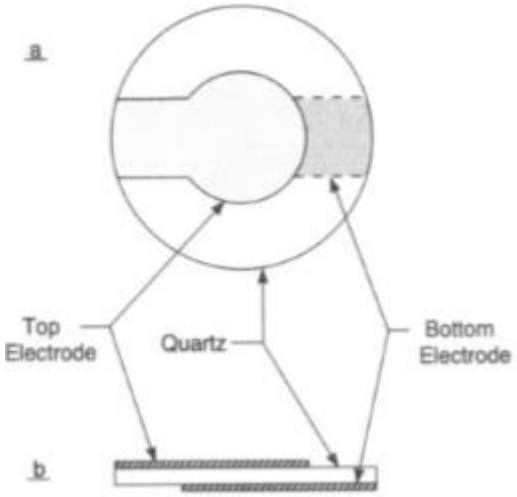

Figure 1-5. Side and top view of an idealized QCM.

Figure 1-5 shows a simplified schematic of a QCM. The electrodes provide the contact necessary for inserting the device in an electrical circuit aimed at providing the electric excitation field. Moreover, they make the resonator thicker at the center than at the rim. The idea behind this design choice is to use the *energy trapping effect* to confine the displacement field in the center and make it small at the edges. This ensures low losses

[4] Strictly speaking, Eq. 3.2 is valid for the thickness shear mode at lowest frequency. There are, in fact, two orthogonal thickness shear modes at different frequencies because of the anisotropic behaviour of quartz. This concept will be deeply covered in section 1.3.

or, equivalently, a high *Q factor*, which is the ratio of frequency and bandwidth (Capelle, et al., 1990)[5].

A QCM exploits the thickness shear mode for detecting mass changes. Sauerbrey showed that a small mass deposit causes a decrease in the initial resonant frequency according to the following equation (Sauerbrey, 1959):

$$\Delta f_n = -\Delta M \frac{2 f_n^2}{A\sqrt{G\rho_q}} \tag{1.5}$$

where Δf_n is the resonance shift, ΔM is the deposited mas change and f_n is the unloaded natural frequency. A, G, ρ_q are parameters describing the microbalance: respectively the electrode area, the quartz torsional modulus of elasticity and the density. The equation was obtained under the hypothesis that the mass deposited on the microbalance is a circular quartz disk with same area of the electrodes.
Eq. (1.5) is also referred to as *mass loading effect*. It is valid for frequency shifts smaller than 2% of the initial resonance. After this limit, the equation becomes non-linear and corrections must be introduced (Lu, 1974).
The equation shows also that high initial natural frequencies lead to higher mass sensitivity. More specifically, a properly designed QCM can detect changes in surface mass density of roughly one ng/cm^2 provided that it is possible to accurately sense frequency shifts of a few Hz (Martin, et al., 1993).

Many design factors influence the resonant condition of the device. Specifically, the most important one is the thickness, followed by the cut, size, shape and quality of the crystal (Hewlett Packard, 1997). In addition, the presence of the electrodes must be taken into account. Because of these many variables, spurious modes usually appear (Haruta & Spencer, 1966). This is shown in the example of a quartz disk's frequency response function of Figure 1-6.

[5] Equivalently, the *Q factor* is also interpreted as the ratio of total energy and elastic losses during vibration. Values for a standard QCM are between 10^5 and 10^7 (Wu, et al., 2003).

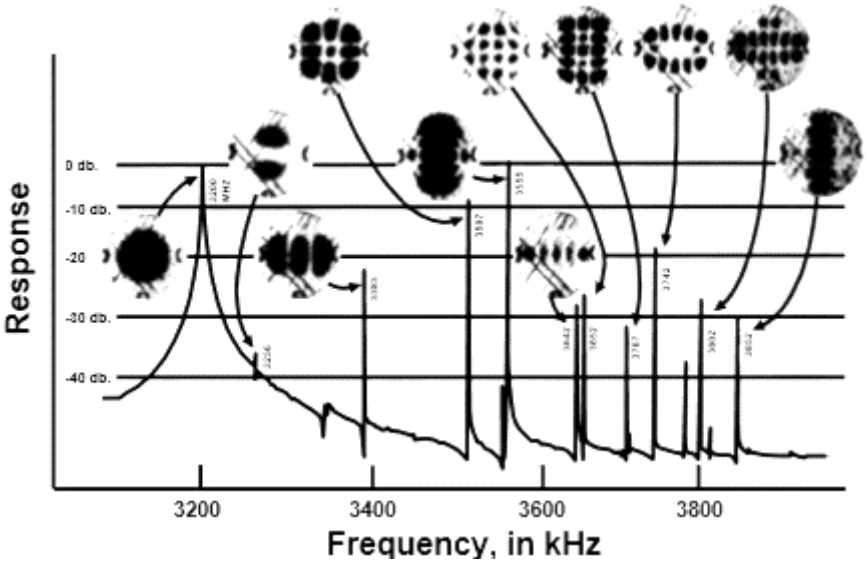

Figure 1-6. Example of FRF and X-Ray topography of excited modes (Vig, 2004).

The first pick denotes the principal TSM. This conclusion can be drawn by looking at the deformation shape, which is uniform (the entire disk is dark colored). Aim of a correct design is to work at that specific frequency (3.2 MHz in the example).
The other visible picks indicate the presence spurious modes. They are in general not critical since they take place at frequencies sufficiently far from the main one so that coupling with the TSM does not happen.
Nonharmonic overtones, on the other hand, are undesirable as they may lead to the generation of unwanted signal corruption, thus decreasing the accuracy of the measurement. They are visible in the small wavy parts of the response curve. Strict design rules are used to minimize these unwanted modes.

The frequency detection is critical when operating a QCM. Many factors influence the frequency stability of a resonator. Figure 1-7 illustrates examples of the major oscillator instabilities.

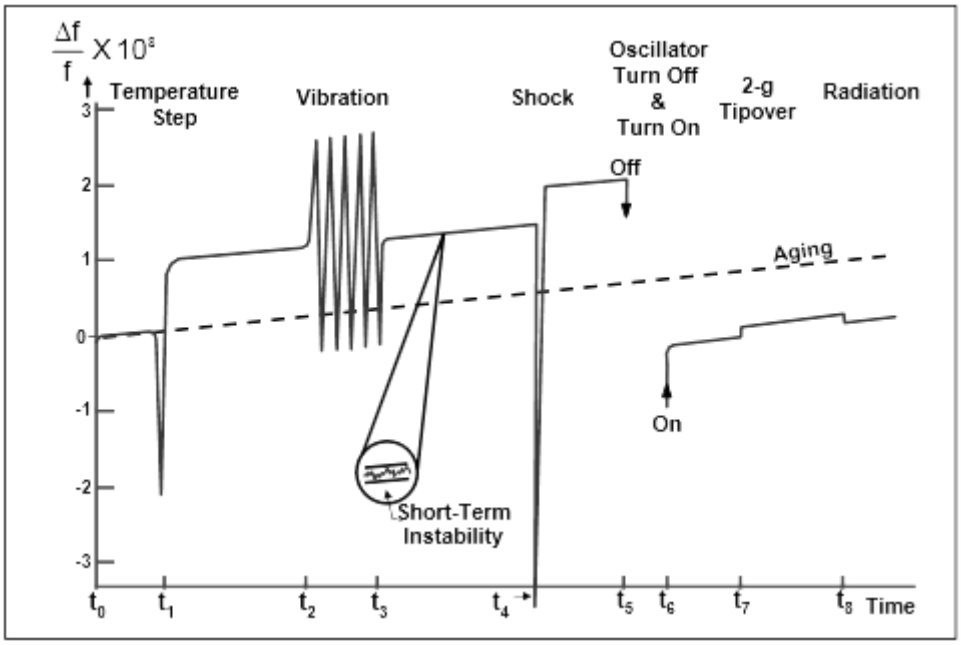

Figure 1-7. Oscillator instabilities due to temperature and their time dependency (Vig, 2004).

It can be seen that a step in the working temperature or a thermal shock can cause instantaneous instabilities. On the other hand, aging, short-term instabilities and thermal fluctuations are time dependent phenomena.
Aging, according to the definition internationally adopted, is a systematic change in frequency with time (CCIR, 1990). The main causes of aging appear to be mass transfer to or from the resonator surfaces (due to adsorption and desorption of contamination) and stress relief within the mounting structure or at the interface between the quartz and the electrodes (Meeker & Vig, 1991). Therefore, in order to achieve low-aging, crystal units must be fabricated and hermetically sealed in ultraclean, ultrahigh vacuum environments.
Short-term instabilities are essentially synonymous of noise. Temperature fluctuations, random vibrations, thermally induced charge fluctuations (Johnson noise) and electrical circuit defects are all possible causes. Thermal loads, hysteresis (Kusters & Vig, 1989) and thermal shocks also affect the frequency-temperature-time response of the QCM (Ballato & Vig, 1978).

A stress field is another important source of frequency changes. There are varieties of stresses built, inadvertently, into a newly manufactured resonator. They might be caused by thermal expansion coefficient local differences, residual strains in the quartz or in the electrodes, mounting or bonding operations (Kusters, 1985).

Accelerations (gravity, shock, and vibrations) (Filler, 1988), iodizing radiation (Capone, et al., 1970), atmospheric pressure and humidity have to be considered, among the other factors, with particular attention in some specific applications (Vig & Walls, 1994).

For this reason, even the most accurately designed QCM suffers from disturbances when operating in practice.

1.3 On the anisotropy of quartz

Quartz is a highly anisotropic material, i.e. some physical properties depend on the direction in which they are measured.

The stress-strain behavior is described by a fourth order tensor. The Voigt notation is used in this thesis to switch from tensors to matrix algebra and simplify the notation. Thus, the linear elastic behavior is described by a full 6x6 matrix and, considering that the latter should be symmetric, twenty-one coefficients are needed to fill it completely. In the specific case of quartz, however, it is known that only six elastic coefficients are needed. This is the result of its trigonal lattice (Vannucci, 2008). Hooke's law becomes the following

$$\underline{\sigma}=\begin{bmatrix} C_{11} & C_{12} & C_{13} & C_{14} & 0 & 0 \\ C_{12} & C_{11} & C_{13} & -C_{14} & 0 & 0 \\ C_{13} & C_{13} & C_{33} & 0 & 0 & 0 \\ C_{14} & -C_{14} & 0 & C_{44} & 0 & 0 \\ 0 & 0 & 0 & 0 & C_{44} & C_{14} \\ 0 & 0 & 0 & 0 & C_{14} & C_{66} \end{bmatrix} \underline{\varepsilon} \tag{1.6}$$

where the values can be found in literature (Ward, 1992; Vig, 2004; Bechmann, et al., 1962). Notice also that among the six coefficients, only five are independent since

$$C_{66} = \frac{1}{2}(C_{11} - C_{12}) \tag{1.7}$$

As mentioned earlier in this chapter, a base change on Eq. 1.6 is necessary to get properties that are coherent with the cut under investigaton. The coefficients found in litterautre are, in fact, referred to the optical axis (not the ones of the cut under study).

Figure 1-4 sows that the optical axes (X and Y) are not perpendicular to the quartz disk. In order to switch to a local coordinate system where Z' and Y' are perpendicular to the disk, a base rotation of (90-35,25)° along X was performed. Details on the mathematics behind this operation can be found in the code of ANNEX A.

For example, at 23° C the matrix after rotation becomes the following

$$[E] = \begin{bmatrix} 87.49 & 27.07 & -8.93 & 3.36 & 0 & 0 \\ 27.07 & 102.84 & -7.34 & -9.89 & 0 & 0 \\ -8.93 & -7.34 & 130.36 & -5.44 & 0 & 0 \\ 3.36 & -9.89 & -5.44 & 38.73 & 0 & 0 \\ 0 & 0 & 0 & 0 & 29.36 & -2.14 \\ 0 & 0 & 0 & 0 & -2.14 & 69.25 \end{bmatrix} \quad (1.8)$$

where all the values are expressed in GPa.

A similar thing was done for the thermal expansion coefficient. Details can be found in literature (Ward, 1992; Kosinski, et al., 1992). Obviously, a physical quantity such as density does not require any transformation.

In the articles cited in this section also the temperature dependence of these parameters is addressed. Further details will be provided later on in this work.

1.4 On the VISTA instrument

Thermogravimetric analyses (TGA) are extensively popular in science and engineering. Their aim is to study condensation/sublimation and absorption/desorption processes, with a wide range of applications, from studies on particulates in Diesel engines exhaust gas (Cuthbertson, et al., 1979) to CO_2 capture by solid solvents (Anon., 2007). The basic instrumental requirements for thermogravimetric analysis are a precision balance and a furnace (Coats & Redfern, 1963). The goal is to measure a mass change during a specific temperature cycle (Mamleev & Bourbigot, 2005). In such a way, volatile components' desorption can be inferred, as well as the chemical composition (from enthalpy of sublimation).
VISTA (*Volatile In Situ Thermogravimetry Analyzer*) is specifically intended for thermogravimetric analyses in space. The main innovation is that the device uses a QCM equipped with a built-in heater, instead of traditional precision balances and

furnaces. This scheme strongly optimizes both the total mass and the power required to perform thermal cycles (Palomba, et al., 2012). The design of the microbalance, along with its mounting system, is discussed in previous literature (Scaccabarozzi, et al., 2014) and is shown in Figure 1-8.

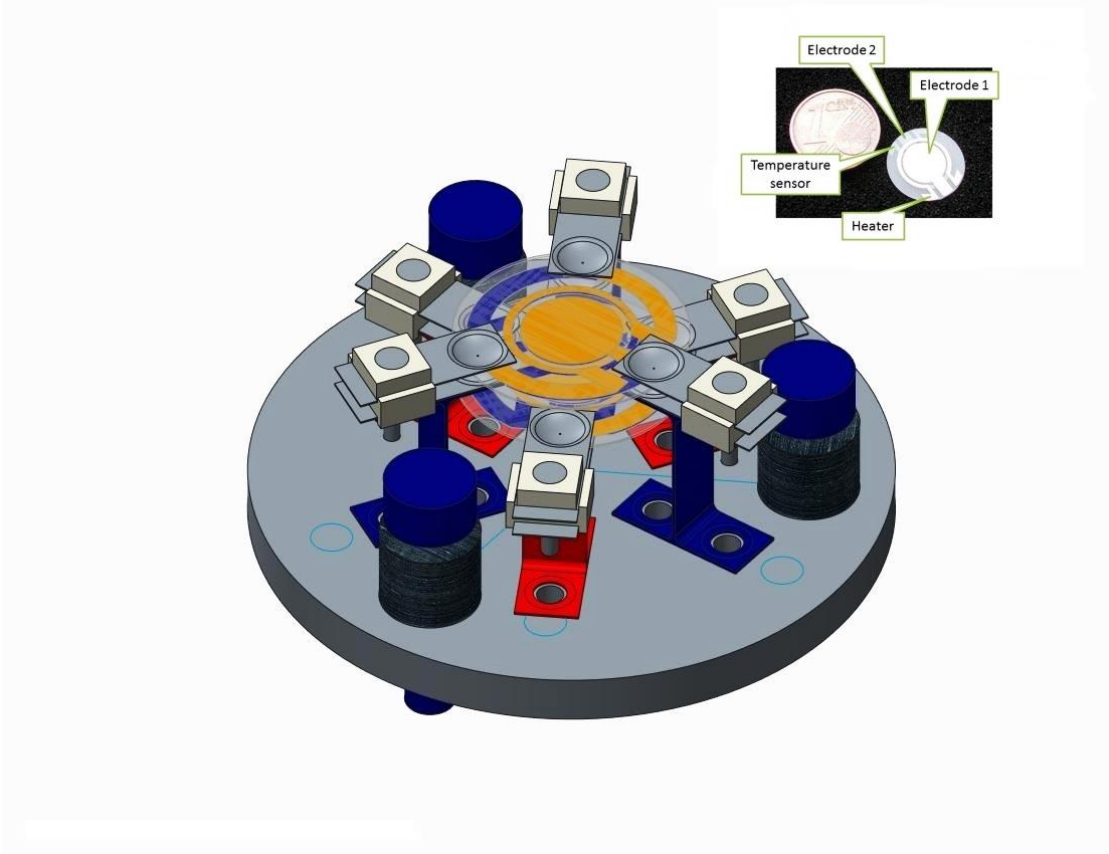

Figure 1-8. QCM for VISTA instrumentation. Size comparison with a 1-cent coin.

VISTA instrument is under study for different space programs:

- *MarcoPolo-R*, is a sample-return mission targeted at near-Earth asteroid 341843 (2008 EV5). Such samples would provide important information on materials and processes in the early solar system, on the formation of the terrestrial planets and on the delivery of carbon-bearing compounds to the early Earth (Barucci, et al., 2013).
- *JUICE* (Jupiter Icy Moon Explorer) aims at investigating Jupiter and its system, with particular attention to Ganymede as a planetary body and potential habitat. The characterization of the ocean layers and detection of putative subsurface

water reservoirs, topographical mapping of the surface and the study of the physical properties of the icy crusts are among the primary objectives (ESA, 2012).

- Other *in situ* applications on Mars, Moon and extra planetary environments or asteroids are possible as well (Palomba, et al., 2012).

1.5 Scope of the thesis

The effects of temperature on a TSM device have been discussed from a wide perspective (section 1.2). However, the articles previously cited deal with a uniform temperature distribution. As for the microbalance under study, it is known that it operates under a non-uniform thermal field when heated. This fact is a consequence of its innovative heater design, which provides power to the adjacent crystal areas by conduction (Fig. 1 8). For this reason, understanding the effect of a non-uniform thermal field on the microbalance is a topic of high interest, both theoretically and practically.

This thesis examines the effects of temperature gradients on the microbalance both in static and dynamic conditions. First, a thermoelastic analysis is conducted to assess the stress-strain behavior of the device in stationary conditions. The focal point of this part of the research is to get information on the deformed shape of the crystal and to measure the stress values on it. Secondly, the study outlines the effects of a non-homogeneous temperature field on the crystal's thickness shear modes with particular care for the frequency values and mode shapes.

CHAPTER 2

This chapter discusses the experimental phase of the thesis aimed at providing and measuring a thermal field on the microbalance. First, an overview of the testing procedure is proposed, justifying and briefly explaining the techniques adopted. Then, the dissertation gets more detailed; each phase of the experiment, along with the results yielded, is separately addressed. Finally, the finite element procedure is explained.

2.1 Overview of the experimental phase

Figure 2-1 displays a sketch of the microbalance's upper face as given in previous literature (Scaccabarozzi, et al., 2014).

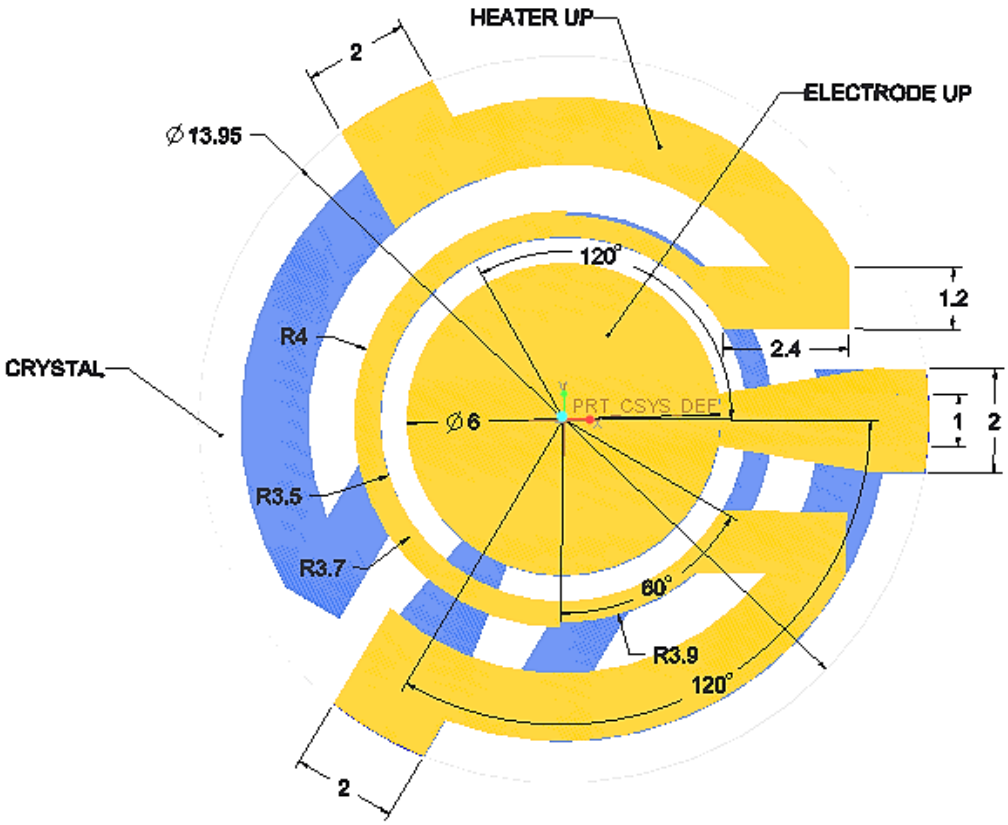

Figure 2-1. Microbalance's upper surface with dimensions. Units are in mm.

Electrode plate and heater circuit are highlighted (yellow). The 120° angular shift between electrodes pads ensures crystal efficiency. This also leads to symmetry; the design is, in fact, symmetrical with respect to a perpendicular plane (with respect to this page) cutting the crystal in half. The crystal has a thickness (not shown in the figure) of 0.167 mm, while the deposited layers are 0.16 μm thick. Deposit design for the bottom face is the same, except for a different orientation of both electrode and heater (Figure 2-2).

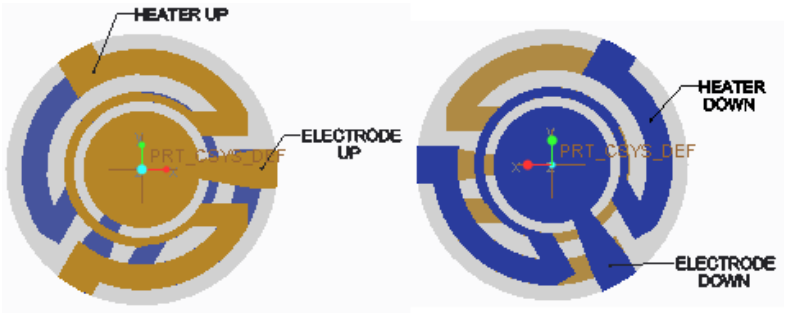

Figure 2-2. Left: Upper face. Right: Lower face.

The diameter of the crystal is 13.95 mm. The thickness is two orders of magnitude smaller than the diameter. Clearly, the device is very thin hence extremely sensitive to contact (see also Figure 1-8). Moreover, any defect, scratch or dirt left on the crystal can significantly alter the principal vibration mode, thus affecting the overall QCM accuracy (not to mention the damaging effect they can have). The obvious conclusion is that a non-contact measurement must be performed to get temperature data during the experimental tests in order to avoid any detriment to the device. For the purpose of this thesis, infrared thermography (IRT) was the adopted technique.

IRT uses a thermographic camera to detect radiation in the infrared range[6] of the electromagnetic spectrum. The power density [W/m^2] emitted by a body depends on the temperature according to the Stefan-Boltzmann law

$$W = \frac{\epsilon \sigma T^4}{f} \tag{2.1}$$

where ε is the emissivity, σ is the Stefan-Boltzmann constant [$5.67 \cdot 10^{-8}$ $W/(m^2 K^4)$], f is the view factor and T is the absolute temperature. Thus, all bodies above the absolute zero emit radiation. IRT cameras work with a device, usually a microbolometer (Kesim,

[6] More specifically, long-infrared wavelengths (from 9 to 14 μm).

et al., 2014) or a photonic detector (Kolahdouz, et al., 2012), able to sense radiation. Then, by knowing the power density and inverting Eq. 2.1, temperature data can be inferred.

The intrinsic problem of this procedure is that emissivity and view factor are in general not known. The first parameter varies from zero (non-emitting body) to one (*black body*[7]) and it is an index of how much radiating energy a body can emit with respect to the maximum possible at that particular temperature. It depends on many parameters, among which, material, body shape, surface roughness, temperature and radiation wavelength are the most important ones (Incropera & De Witt, 2011). For this reason, the first task of the experimental activity of the thesis was devoted to the characterization of the microbalance's emissivity.

The view factor depends on the geometry and the relative position of two surfaces exchanging radiation. It does not depend on temperature nor on surface properties of the body. It has been computed for many cases and it is in general given in numerical or tabular form (Cengel & Ghajar, 2011). Concerning the experiment, the view factor was set equal to one, since crystal's surface is flat and it exchanges radiation with the environment only[8]. Hence, after determining the emissivity, Eq. 2.1 was used for measuring the thermal field on the heated microbalance.

Then, the temperature-induced stress field was detected. The latter is expected to appear since the expansion of the crystal is restricted by the supports (Figure 1-8). Several papers in literature deal with the measurement of stress in thin films (Klokholm, 1969; Paesler & Fritzsche, 1974; Budyansky, et al., 2011). Their basic principle is to get curvature data, from which the stress field is then deduced. However, the main problem is that, in general, these techniques require a very complex apparatus, sometimes also expensive. In this thesis, the adopted strategy was to use a finite element analysis (FE). The idea is to reproduce the testing conditions on a thermal FE model and extract the temperature field. If the result is consistent with the experimental data coming from thermography, a thermo-elastic analysis is performed to get the stress field; otherwise, the model and/or the experimental test must be checked. This approach is simple, fast and allows double-checking the data from IRT. In this sense, FEM and IRT provide support to each other. A graphical representation of the overall procedure is presented in Figure 2-3.

[7] A black body is an ideal object able to absorb all the impinging radiation and emit the maximum possible radiating energy at a given temperature.
[8] Or, equivalently, the sample is fully enclosed by the environment (eFunda, 2015).

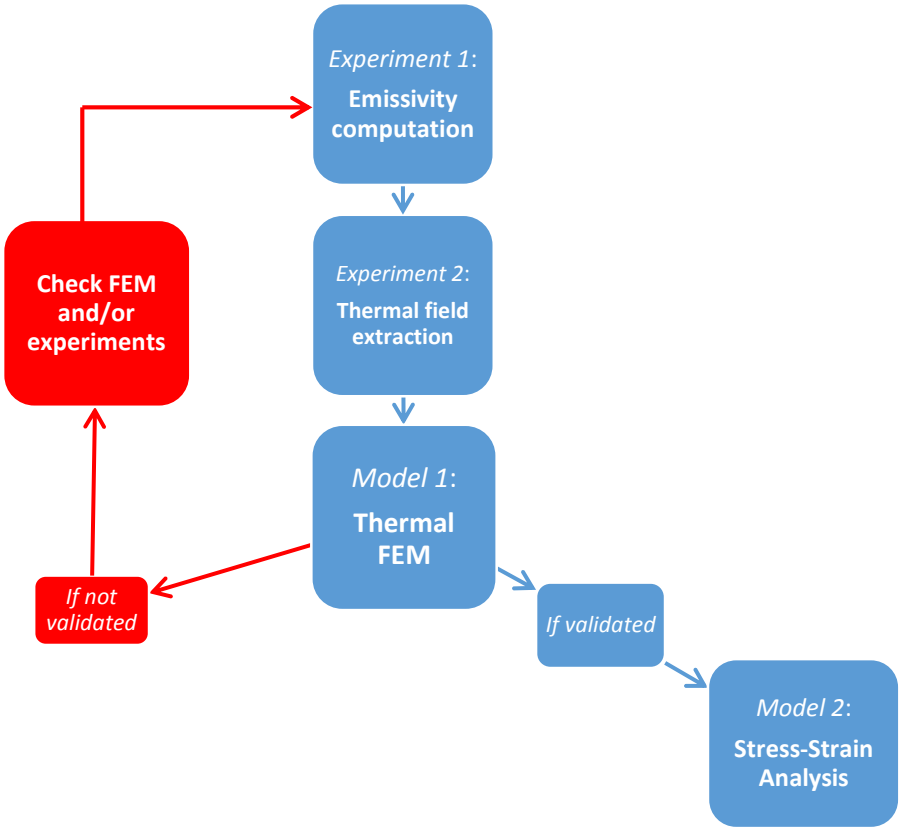

Figure 2-3. Schematic of the experimental procedure.

2.2 Characterization of emissivity

The experimental procedure aimed at measuring the crystal's emissivity consisted in the following phases:

- Providing a known power to a QCM crystal sample;
- Measuring the reached (real) temperature with a low uncertainty device;
- Using IRT to detect radiation emitted, assuming black body behavior;
- Developing a model able to compare the IRT data and the real temperature, in such a way that the emissivity is the only unknown.

Each of the points is addressed in the following sections.

2.2.1 Experiment set-up and temperature measurement

A quartz crystal sample *similar* to the one incorporated in the QCM device was used. The word 'similar' should be here interpreted with engineering judgment: it denotes not only geometry similarity, but also properties matching. In fact, as pointed out in the introduction, along with temperature there are several other parameters affecting the crystal's emissivity properties, such as the type of material, microstructure and surface roughness. For this purpose, a broken crystal used for preliminary tests was used, since it fully satisfies the similarity demand.
The chosen sample was, then, deeply cleaned, because any trace of dirt has its own emissivity that can mask the crystal's one and increase the uncertainty of the measure. An ultrasound washer, followed by additional manual cleaning with acetone, served the purpose.

Then, power was provided to the sample. Figure 2-4 illustrates the equipment used. The power supply allows the user to set a given voltage to a wire; energy, in the form of heat, is then released because of *Joule heating*[9].

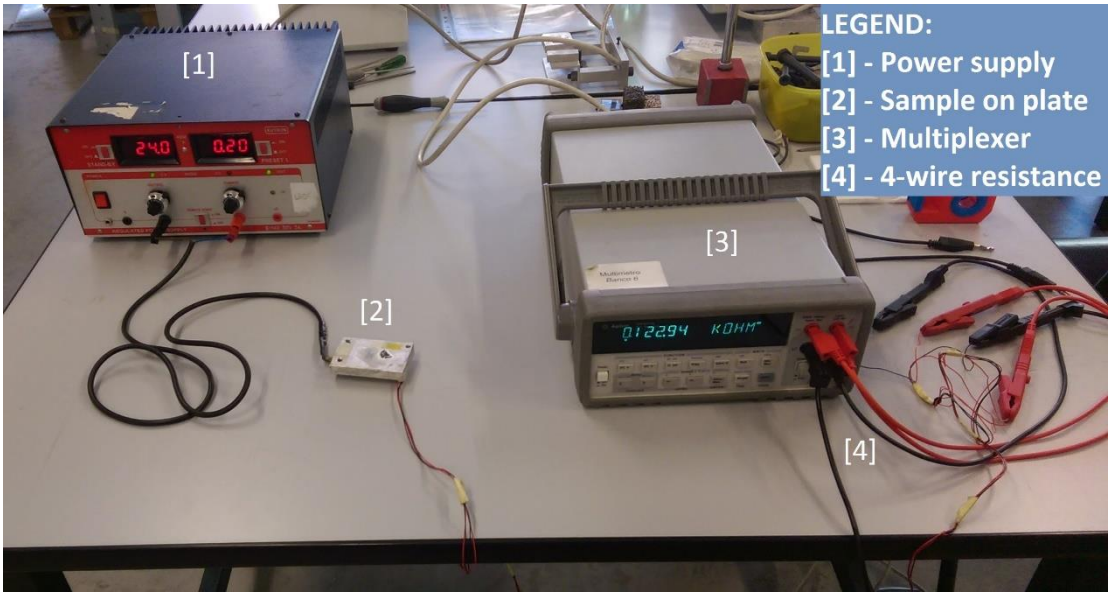

Figure 2-4. Set-up of the experiment for emissivity characterization.

[9] Joule heating is the process by which the passage of an electric current through a conductor releases heat. The amount of heat released is proportional to the square of the voltage; $^1/_R$ is the constant of proportionality.

The sample was fixed on a conductive plate by means of some thermal grease, so that temperature equivalence is achieved between plate and crystal. Moreover, the plate was surrounded by some polystyrene bricks (not shown in the figure) in order to block any direct external impinging radiation. The voltage was set to be 24 V (see the power supply display on the left).
The basic idea is that if steady state condition is reached, the conductive plate and the crystal above it are in thermal equilibrium i.e. are at the same temperature. The latter was, then, measured. A 4-wire resistance (PT 100 A-class) was used; it gave as output the circuitry resistance (see the multiplexer display in Figure 2-4) which was manually transformed into a temperature value by means of conversion tables[10]. Concerning the experiment, the resistance value was found to be 126.14 Ω (after waiting for steady state). This exact value was not present on the table used; thus, linear interpolation between the two adjacent resistance values (125.923 and 126.306 Ω) was performed, as shown in Table 2-1.

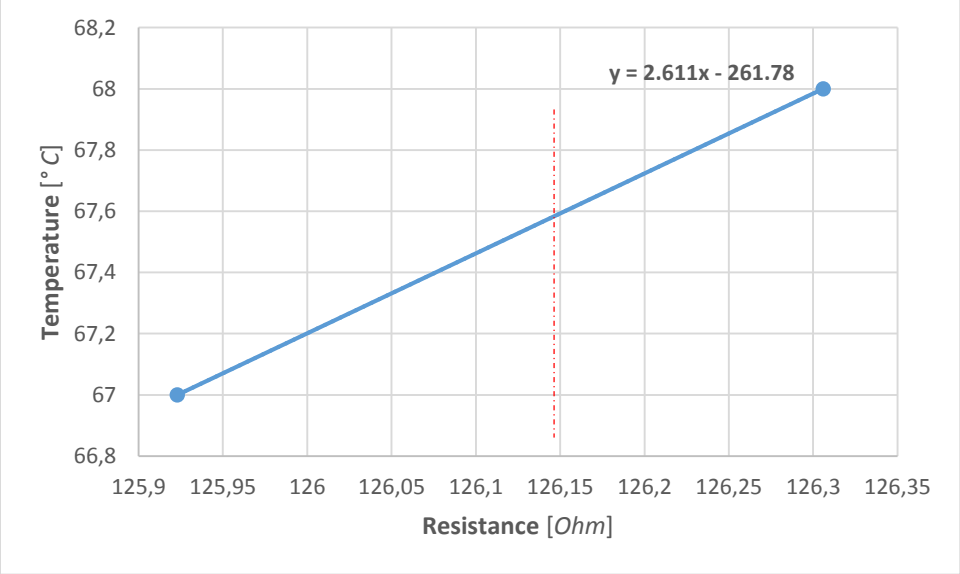

Table 2-1. Calibration curve for PT100 temperature measure.

As a result, a temperature of approximately 67.6 °C was estimated.

The uncertainty of the measure depends on the class of the instrument and on the measured temperature. It can still be found in literature or internet databases in tabular form (see note 10). Concerning the experiment, tables indicated that uncertainty was between 0.15 and 0.35 °C, respectively at measured temperatures of 0 and 100 °C. The

[10] Tables used were taken from http://www.nist.gov

process of linear interpolation was used, once again, to extract a single estimate. It was concluded that the uncertainty of the temperature measure was equal to 0.28 °C.

2.2.2 Infrared imaging on the sample and results

A T640 FLIR thermographic camera was used to detect radiation emitted by the heated sample. The following two important assumptions are worth to be noted:

- Atmosphere corrections were not introduced, simply because the sensing device and the sample were put close enough (50 cm) so that air transmissibility could be considered unitary. For longer distances, air and its molecules could be obstacles on the radiation path to the instrument thus affecting the whole measuring process (Fowle, 1919);
- Black body behavior of the crystal was assumed. This is consistent with the fact that emissivity is the unknown.

Figure 2-5 shows the image of the heated crystal sample from IRT.

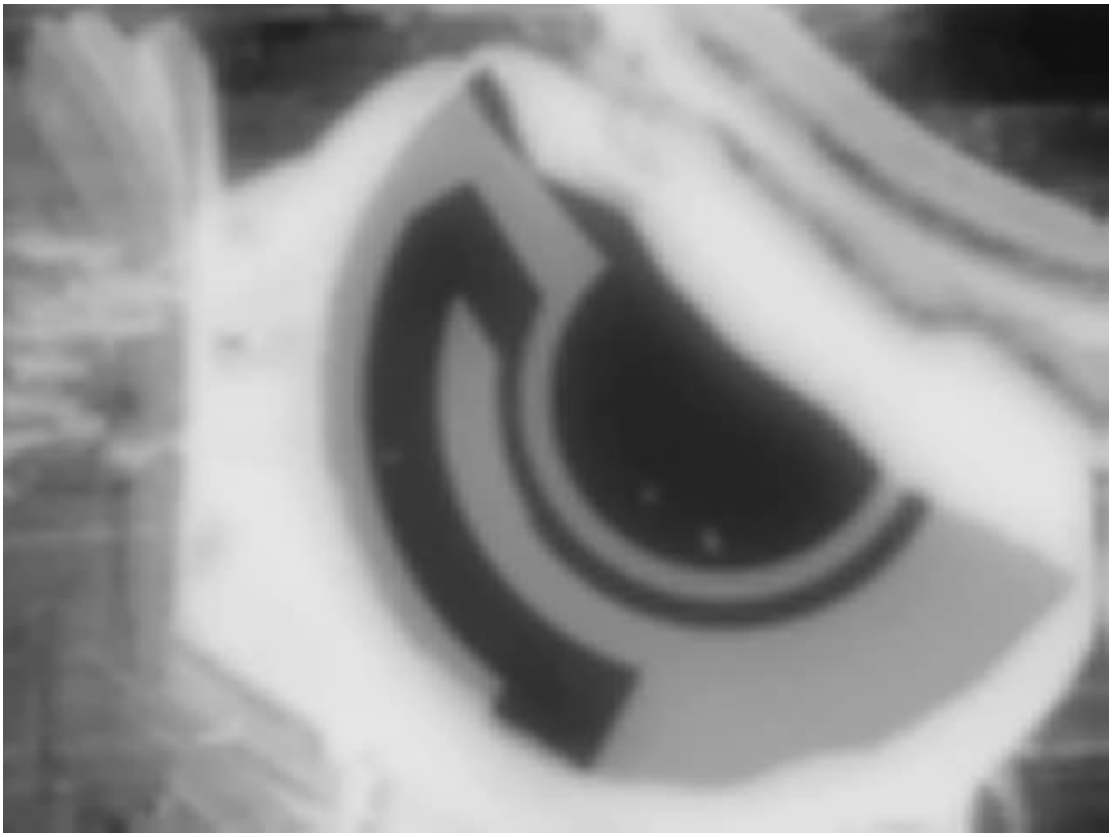

Figure 2-5. Sample seen from the infrared camera.

The picture is in grayscale colors: dark areas correspond to low radiating energy sensed (vice versa for bright areas). The infrared camera also indicated the minimum and maximum temperatures of the scale, respectively of 30.3 and 69.9 °C.
Figure 2-5 is an 8-bit image[11], i.e. an array of numbers ranging from zero to 255. The grayscale color map is just a way to visualize those values: number zero (minimum temperature) is displayed as black, while 255 (maximum energy sensed) as white. Intermediate values are shown in levels of gray; the latter are linearly related to the impinging radiation.
It is clear that, no temperature data can be directly be read in the image. A process of conversion from numbers indicating grayscale levels to actual temperature data was performed. A MATLAB® script was developed for this purpose (see ANNEX B). Its basic idea is to apply a linear transformation expressed by the following equation.

$$T_{ij} = N_{ij} \frac{T_{max} - T_{min}}{255} + T_{min} \tag{2.2}$$

[11] If *n* is the number of bits, the gray levels are 2^n - 1.

where T is the temperature in Celsius degrees and N is the color level number from the image. Notice that the formula must be applied to each of the pixels in the 480x640 image; thus $i = 1,2,\dots,480$ and $j = 1,2,\dots,640$.
The following figure shows the temperature field resulting from the coded computations.

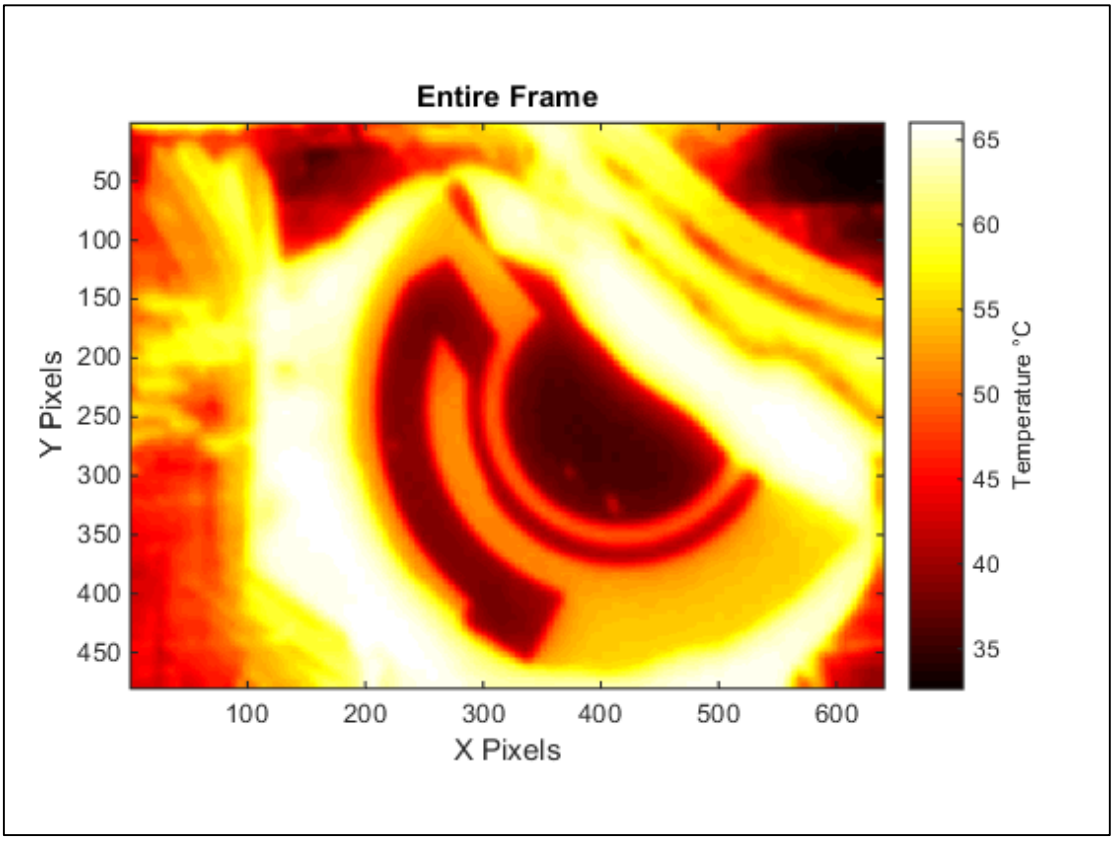

Figure 2-6. Temperature map as extracted from MATLAB code.

Results highlighted in Figure 2-6 are not conclusive yet for two reasons. First, the sample emissivity was assumed unitary and this is never the case for real bodies. Second, the background effect was not compensated.

2.2.3 Background correction and emissivity map extraction

Figure 2-7 is a schematic of the experiment displaying all the energy terms involved.

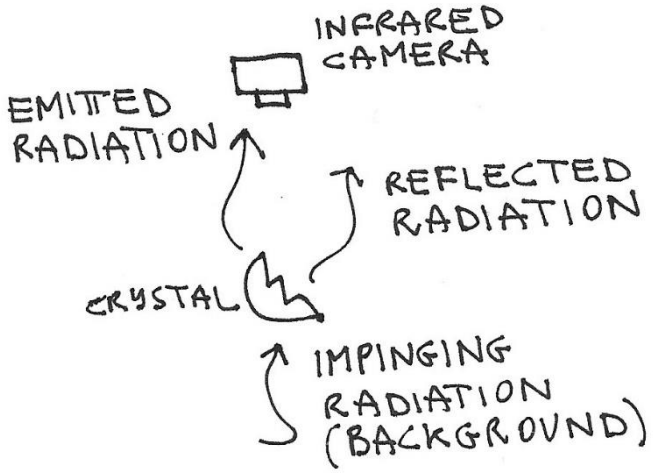

Figure 2-7. Energy model for the experiment.

The energy that the infrared camera senses is the sum of the one directly emitted by the crystal because of its temperature and the radiation from the background that is reflected by the crystal.
In power domain, Eq. 2.1 can be used to describe the directly emitted radiation. A deeper discussion is, however, necessary for the reflected one. First, the *reflection coefficient* should be introduced. It is the ratio of reflected energy and impinging one.

$$\rho = \frac{W_{ref}}{W},\ 0 \leq \rho \leq 1 \tag{2.3}$$

It quantifies the capability of a material to redirect thermal energy. In a similar manner, the *absorption* and *transmission* coefficients can be defined[12]. The picture below clarifies the meaning of these coefficients.

[12] Please note that the definitions given above are not restricted to the infrared portion of the energy spectrum. For this reason, some authors refer to them as *monocrhomatic coefficients*. For more details, see 'Cengel & Ghajar, 2011'.

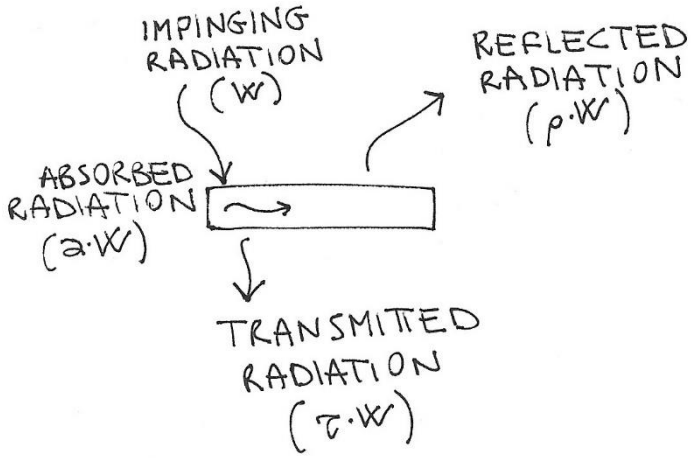

Figure 2-8. Side view of the crystal.

It is known, from the first principle of thermodynamics, that the sum of absorbed, reflected and transmitted radiation is equal to the impinging one. Thus,

$$W_{abs} + W_{ref} + W_{tr} = W \tag{2.4}$$

By dividing both members by *W*, the following relation is obtained

$$\alpha + \rho + \tau = 1 \tag{2.5}$$

where α, ρ and τ are respectively the absorption, reflection and transmission coefficients.
The sample was assumed to behave like a perfect opaque surface (Santos, et al., 2013) so that τ was set to zero. Therefore,

$$\alpha + \rho = 1 \tag{2.6}$$

Eq. 2.6 links the reflection and absorption coefficients. The latter is, however, an unknown. Kirchhoff's law was introduced to deal with this issue (Eq. 2.7).

$$\epsilon(T) = \alpha(T) \tag{2.7}$$

The equation states that the emissivity and absorption coefficients can be considered equal given that there is no big temperature difference between the surface absorbing energy and the radiation source. In the experiment, the crystal surface temperature was 67.7 °C while the surroundings' one was 22.7 °C (measured by RTD). Since the

temperature difference is below 100 °C, Kirchhoff law can be applied with no need to correct it. With these assumptions, the reflection coefficient was expressed as a function of the emissivity. In fact, the combination of Eq. 2.6 with Eq. 2.7 yields the following result:

$$\rho = 1 - \epsilon \tag{2.8}$$

With regards to the energy model in Figure 2-7, the following power balance can be written:

$$\sigma\epsilon_{th}T_{th}^4 = \sigma\epsilon_m T_m^4 + \sigma(1-\epsilon_m)T_{bk}^4 \tag{2.9}$$

where the suffix '*th'* refers to the infrared camera, '*m'* to the microbalance and '*bk'* to the background.
The first member quantifies the radiation sensed by the infrared camera (Eq. 2.1). The second member is the sum of two contributions (again using Eq. 2.1): the power directly emitted by the crystal and the one coming from the background then reflected. Notice that the reflection coefficient has already been introduced in the form given by Eq. 2.8. Moreover, is worth to be noted that the Stefan-Boltzmann constant does not play any role because it can be eliminated from the equation.
By remembering that ε_{th} was assumed to be unitary, is clear that the only unknown of Eq. 2.9 is the sample emissivity. Therefore,

$$\varepsilon_m = \frac{T_{th}^4 - T_{bk}^4}{T_c^4 - T_{bk}^4} \tag{2.10}$$

The above equation was used to extract the emissivity values out of the acquired thermal image.

Since T_{th} is a matrix (the image coming from the infrared camera), while T_{bk} (22.7 °C) and T_c (67.7 °C) are scalar values, the result of Eq. 2.10 is a matrix, the so-called *emissivity map*. A MATLAB® script (see ANNEX C) served the purpose of solving the equation and displaying the results (as well as performing other calculations that will be addressed later).

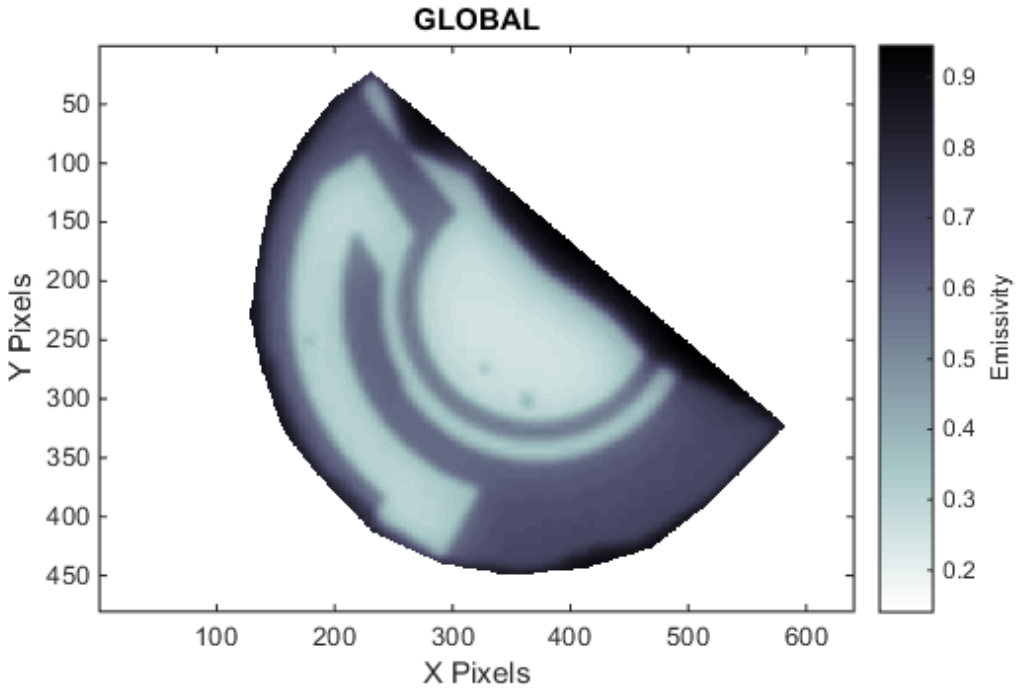

Figure 2-9. Crystal's emissivity map.

Figure 2-9 shows the emissivity map. Dark areas are regions of high emissivity, i.e. close to one (vice versa for the bright ones). It can be seen that the sample has regions of different emissivity corresponding to the dissimilar emitting materials: the electrode and the heater, in particular, show low values since they are made of a highly reflective material (chromium-iron alloy with gold coatings). The quartz crystal, as expected, has a higher emissivity.

Moreover, some emissivity gradients are present within areas of homogeneous emitting material. This can be expected by a temperature that is not uniformly distributed. However, these differences appear to be more the result of a local bias in the experiment than the normal behavior of emissivity. Figure 2-10 shows, for instance, a contour plot of emissivity on the electrode area.

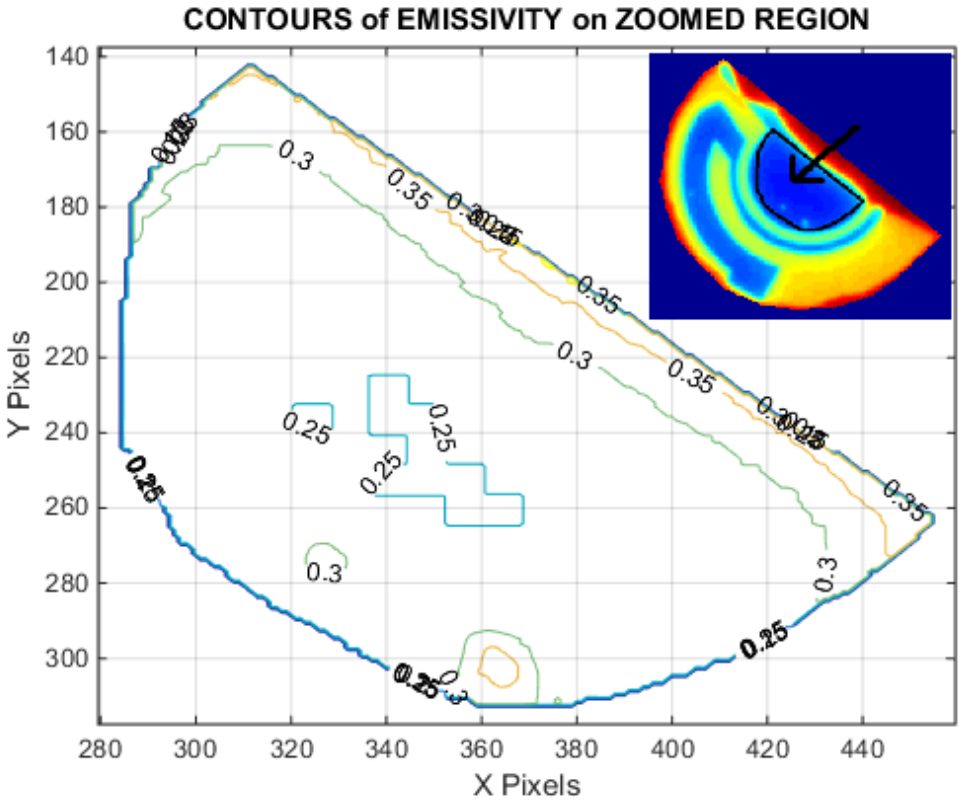

Figure 2-10. Contour of emissivity on electrode area.

It can be seen that there are two different types of gradients. In particular, the ones near the borders of the electrode area are due to the so-called *edge effect*: the presence of two different emitting sources placed one close to the other makes the emissivity value blur at the boundary. In this very case, the thermal grease diffuses so much energy in every direction that the pixels near the sample edge are affected by it. For this reason, the emissivity values close to the thermal grease are not trustworthy.
Instead, the circular contour lines inside the area are probably caused by localized dirt, surface scratches or material heterogeneities. Nevertheless, as pointed out in the introduction, it is very difficult to understand the reason for these local behaviors because many factors play a role in determining the emitting property of an object. For example, it could be possible that the thermal paste used in the experiment was not uniformly distributed below the sample (Figure 2-11) or some voids could have been present.

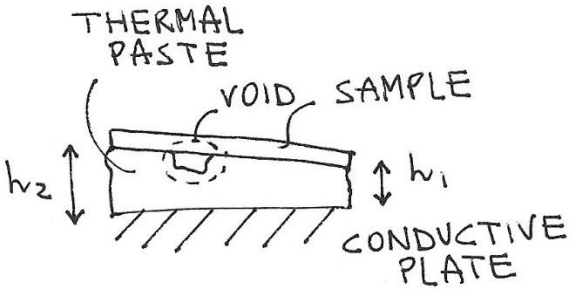

Figure 2-11. Cross-section of the sample from the experiment.

An estimate of the materials' emissivity was computed by means of the code of ANNEX C. Results are shown in the following table.

Sample Region	Average Emissivity
Crystal	0.665
Heater	0.309
Electrode	0.264

Table 2-2. Sample emissivity values.

2.2.4 Uncertainty of emissivity

The uncertainty associated with the emissivity estimation of the previous section is of interest in order to understand where the computed values are more trustworthy.
Eq. 2.10 shows that the emissivity is a function of the temperature coming from the IRT, as well as the background and sample temperatures. In a simpler form, it can be written that

$$\varepsilon = \varepsilon(T_{th}, T_{bk}, T_m) \tag{2.11}$$

Thus, the emissivity of uncertainty depends on the uncertainty associated to those temperature values.

As seen in section 2.2.1, a 0.28 °C uncertainty was estimated for the sample temperature. The background one was measured by means of the same RTD and tables quantified a 0.20 °C uncertainty for it. With reference to the infrared camera, the

manufacturer internet site[13] indicated a resolution equal to the two percent of the full scale (150 °C) that is 3 °C. In order to convert this value into an uncertainty, a *type B* approach is used (Doebelin, 2008): a rectangular probability distribution is guessed, thus the accuracy becomes $3/\sqrt{3}$ that is 1.73 °C. It can be noted that this last value is higher than the previous two, thus meaning that the uncertainty of the overall emissivity estimation is deeply influenced by the IRT sensor. This is an intrinsic property of this kind of measurement techniques and must be taken as it is; nothing can be done to enhance it.

In order to propagate the uncertainty from temperatures to emissivity, it is possible to split Eq. 2.10 in a series of simple mathematical operations and use the rules of sum, difference, product and quotient of uncertainties[14]. However, this process is not suggested here since T_{bk} appears on both the numerator and denominator of Eq. 2.10 so this approach does not allow the possibility for the two uncertainties to elide each other (Taylor, 1997).
The method used is as follows. First, independence of the three temperature measures was assumed (this is for sure the case for the experiment). Then, the following formula was used

$$\delta\varepsilon = \sqrt{\left(\frac{\partial\varepsilon}{\partial T_{th}}\delta T_{th}\right)^2 + \left(\frac{\partial\varepsilon}{\partial T_{bk}}\delta T_{bk}\right)^2 + \left(\frac{\partial\varepsilon}{\partial T_m}\delta T_m\right)^2} \tag{2.12}$$

where $\delta\varepsilon$ is the emissivity overall uncertainty, δT_{th}, δT_{bk}, δT_m are respectively the uncertainties of IRT, background and sample temperatures. The partial derivatives in Eq. 2.12 can be analytically computed:

$$\frac{\partial\varepsilon}{\partial T_{th}} = \frac{4T_{th}^3}{T_m^4 - T_{bk}^4} \tag{2.13}$$

$$\frac{\partial\varepsilon}{\partial T_{bk}} = \frac{4T_{bk}^3(T_{th}^4 - T_m^4)}{\left(T_m^4 - T_{bk}^4\right)^2} \tag{2.14}$$

$$\frac{\partial\varepsilon}{\partial T_m} = -\frac{4T_m^3(T_{th}^4 - T_{bk}^4)}{\left(T_m^4 - T_{bk}^4\right)^2} \tag{2.15}$$

[13] http://www.flir.com
[14] When any number of quantities are added or subtracted, the *uncertainties* in those quantities always add. Instead, when quantities are multiplied or divided the *fractional uncertainties* add.

The code of ANNEX C was used to perform the above-mentioned computations. Results are presented in the following figure.

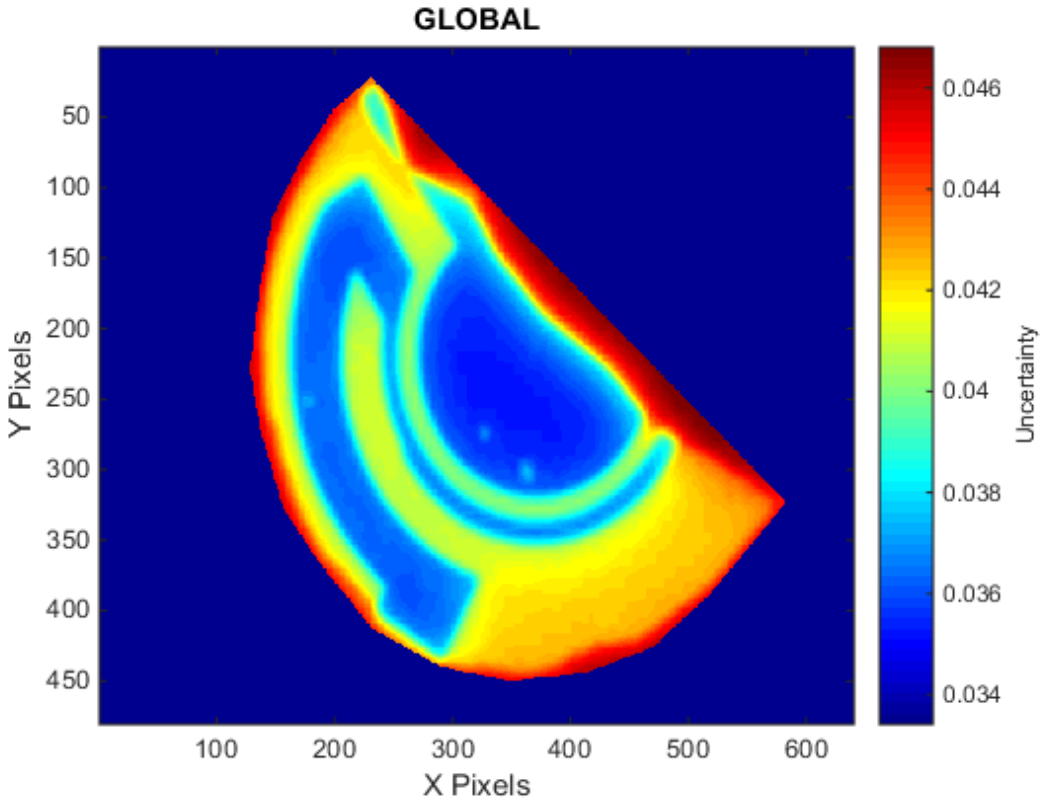

Figure 2-12. Emissivity uncertainty.

Similarly to what previously done for emissivity values, an average uncertainty was computed for each material. Then, the ratio of average uncertainty and average emissivity, i.e. that is the relative uncertainty, was worked out too.

Sample Region	Absolute Uncertainty [°C]	Relative Uncertainty [%]
Crystal	0.042	6.3
Heater	0.036	11.7
Electrode	0.035	13.4

Table 2-3. Uncertainty values.

Table 2-3 shows that the relative uncertainty is smaller in the crystal region. This can be explained as follows. As previously mentioned, heater and electrode reflect a lot of

radiation. This radiation blends with the directly emitted one, thus it is more difficult to separate the two contributions.

The values in Table 2-3 should be interpreted with engineering judgment. As the *guide to the expression of uncertainty (GUM)* recommends, the mathematical approach should always be supported by critical thinking and intellectual honesty. In the experiment, there were many sources of dispersion (edge effect, material properties etc.) and many assumptions were introduced in the model (Kirchhoff law, perfect opaque surface etc.). This makes the 6.3 percent of relative uncertainty likely an underestimation of its real value.

As a result, two important conclusions can be drawn from this section. First, the emissivity data are more reliable in the crystal area. Second, the relative accuracy is not less than 6.3 percent.

2.3 Test on the QCM

After having characterized the emissivity, IRT was used on the microbalance.

First, heat was provided to the device by means of the heater circuitry. Actually, there are two deposited geometries: one is used as heater, the other as sensor. These are fixed on the microbalance, one for each flat surface. However, since the device's thickness is very small and given the high conductivity of the material involved, power (in the form of heat) was delivered to the bottom heater only. In other words, no thermal gradient in the disk axis direction was expected (this hypothesis was checked in the following stage of the study).
On the contrary, the infrared camera captured images of the device's upper surface. Figure 2-13 helps clarifying this idea.

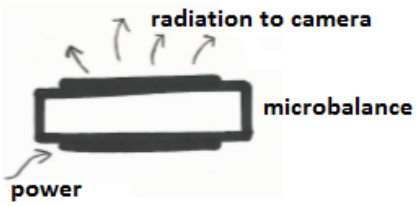

Figure 2-13. Microbalance heating.

The experimental set-up is shown in Figure 2-14. The microbalance was protected from any direct light source so that heat came from the input power only. Moreover, a serial port served the purpose of connecting the heater to an electrical circuit.

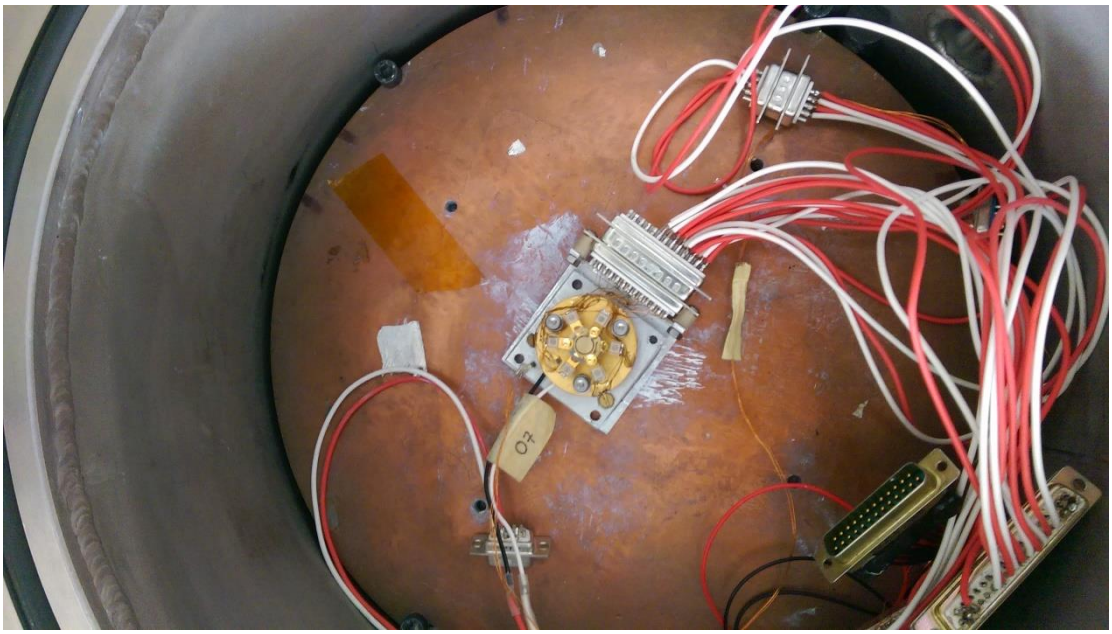

Figure 2-14. Microbalance with serial port and wires.

A power supply provided a voltage to the heater. A multiplexer was set up with multiple channels dedicated to the following purposes:

- Measuring the temperature sensor resistance;
- Double-checking the voltage generated from the power supply (the reason for this need was to avoid any unwanted voltage drop);
- Measuring the current flowing through the heater;
- Multiplying voltage and current to get the power.

Both power supply and multiplexer are not shown in the figure.

The following table summarizes the results after steady state conditions were reached.

Quantity	Value	Unit
Resistance	166	[Ω]

Voltage	9.55	$[V]$
Current	$4.85 \cdot 10^{-2}$	$[A]$
Power	0.464	$[W]$

Table 2-4. Results from acquisition.

The heated microbalance was then analyzed by means of IRT camera. Figure 2-15 shows the captured image.

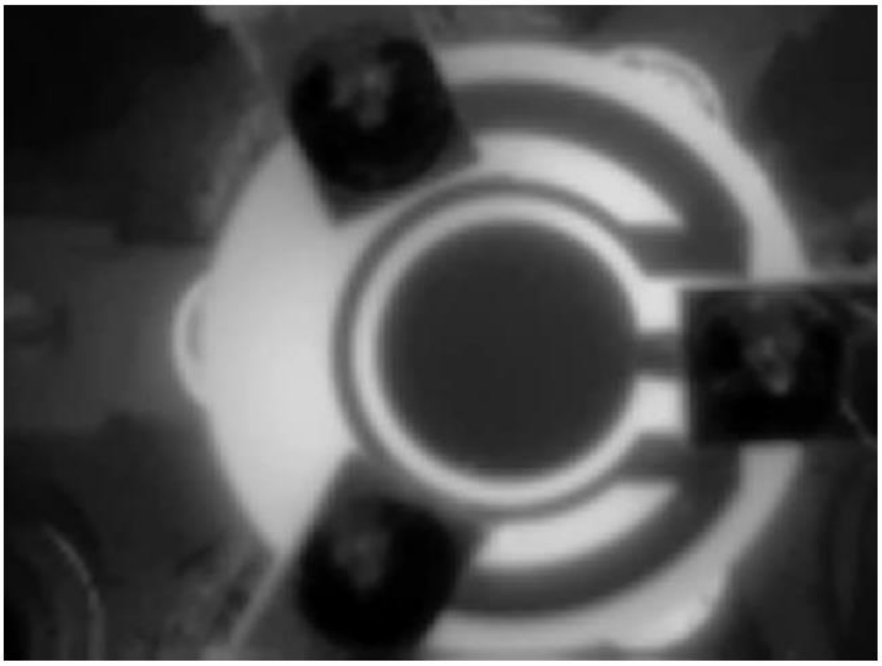

Figure 2-15. IRT on the microbalance.

The camera also indicated the minimum and maximum temperatures of the scale, respectively 24 and 103 °C.

The extraction of temperature data form the above figure follows the same steps discussed in section 2.2.3. The thermal model of Eq. 2.9 was used also in this case. The equation is here reported for simplicity.

$$\sigma \epsilon_{th} T_{th}^4 = \sigma \epsilon_m T_m^4 + \sigma (1 - \epsilon_m) T_{bk}^4 \tag{2.9}$$

However, the way this equation was used is different at this time for the following reasons:

- The temperature from IRT, i.e. T_{th}, is known;
- The emissivity is known from previous computations;
- The background temperature was measured at 22.7 °C.
- The actual microbalance temperature, i.e. T_m, is the unknown.

By solving Eq. 2.9 for T_m, the result is

$$T_m = \sqrt[4]{\frac{T_{th}^4 - (1-\epsilon_m)T_{bk}^4}{\epsilon_m}} \tag{2.16}$$

As previously discussed, the emissivity has a high uncertainty in the electrode and heater regions. Hence, it would not be wise to estimate the microbalance temperature in those areas but rather focus on the crystal, where the uncertainty is lower. The code of ANNEX D was developed to extract regions of interest from Figure 2-15 and compute the temperature map, along with mean, maximum and minimum temperatures. An estimate of the uncertainty is also provided.

For instance, in Figure 2-16, one portion of the crystal area is highlighted by a black line.

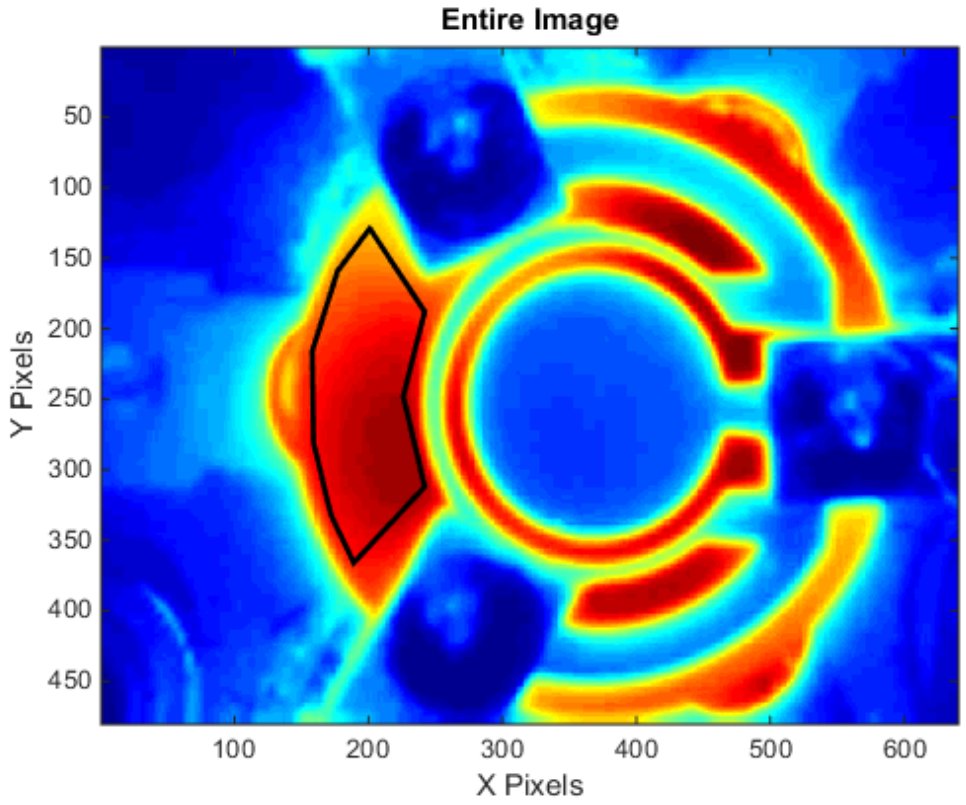

Figure 2-16. Crystal area on QCM.

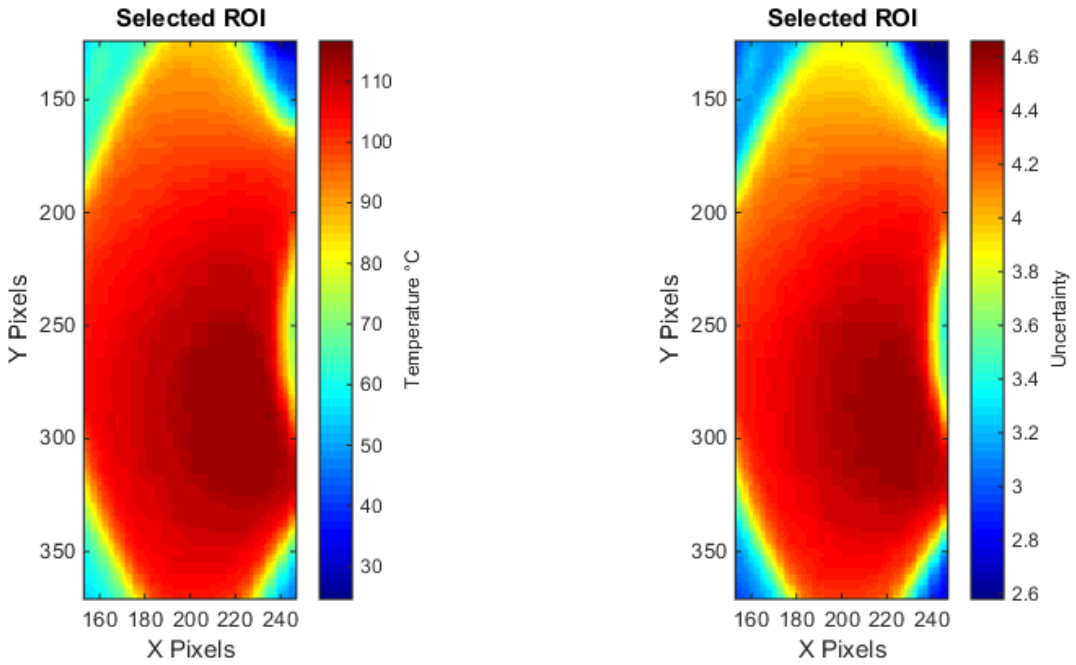

Figure 2-17. Left: temperature values on crystal area. Right: Absolute uncertainty.

Figure 2-17 (left) shows the resulting temperature field. The maximum temperature reached is approximately 114 °C, while the minimum one is around 88 °C. There is a gradient of temperature moving toward the microbalance center, which is visible in the progressively darker red area in the middle of the image.

As for the uncertainty, the propagation of errors method can be applied in the same way shown in the previous section. The derivatives of Eq. 2.16 with respect to the variables T_{th}, ε_m and T_{bk} turn out to be respectively,

$$\frac{\partial T_m}{\partial T_{th}} = \frac{T_{th}^3}{\varepsilon_m \left(\frac{T_{th}^4 + (\epsilon_m - 1) T_{bk}^4}{\epsilon_m} \right)^{3/4}} \tag{2.17}$$

$$\frac{\partial T_m}{\partial \varepsilon_m} = \frac{T_{bk}^4 - T_{th}^4}{4\, \varepsilon_m^2 \left(\frac{T_{th}^4 + (\epsilon_m - 1) T_{bk}^4}{\epsilon_m} \right)^{3/4}} \tag{2.18}$$

$$\frac{\partial T_m}{\partial T_{bk}} = \frac{(\epsilon_m - 1)T_{bk}^3}{\varepsilon_m \left(\frac{T_{th}^4 + (\epsilon_m - 1)T_{bk}^4}{\epsilon_m} \right)^{3/4}} \tag{2.19}$$

Then, the application of Eq. 2.12 yielded the results shown in Figure 2-17 (right). It can be seen that the uncertainty is above 4 °C, thus corresponding approximately to the 4 percent of the measured temperature.

By analyzing other portions of the image, it could be concluded that the maximum temperature reached by the microbalance was around 116 °C with an input power of 0.464 W. This result is in agreement with preliminary measurements in ambient air that showed that to increase the sensor temperature from the ambient value (25 °C) to a value of around 100 °C, the sensor needed less than 0.5 W (Palomba, et al., 2012).

2.4 FEM analyses

In the following section, the FEM analysis is presented. As previously explained, the idea is to develop a model to simulate the temperature field and to extract deformations and stresses from it.
The FEM model is shown in Figure 2-18.

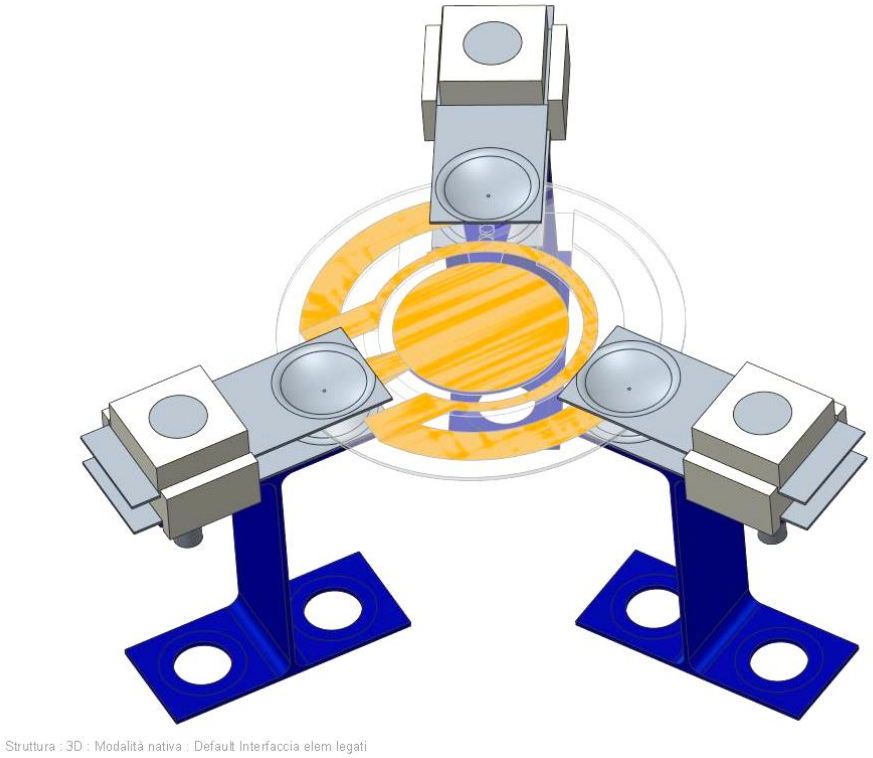

Figure 2-18. FEM model of the microbalance.

Notice how only one crystal sensor out of the two previously shown (Figure 1-8) was modeled. This is in agreement with the fact that only one crystal (the upper one) was heated during the experiment.

2.4.1 Geometry, assembly, material properties and mesh

The geometry is exactly the one previously discussed. However, one major simplification was introduced: the heater and electrode circuitry (in both upper and bottom faces) are not modeled with their own thicknesses and materials. The yellow areas that can be seen in Figure 2-18 are just surface partitions not extrusions. This model choice was made because those parts have a negligible thickness thus they do not contribute much to the overall thermal properties nor they modify the overall stiffness of the device (Valentin, et al., 1984).

Another important point to consider is the contact of crystal and supports. The way it was implemented in the model is as follows: the top of the three supports' sphere-like surfaces were flattened and a rigid link was introduced between the generated contact area and the crystal. A more detailed view of one of these contact surfaces is shown in Figure 2-19. Moreover, a clamping pre-load of 1.3 N was introduced since it is present in the original design (Scaccabarozzi, et al., 2014). In practice, there might be a sliding, but the model did not account for it.

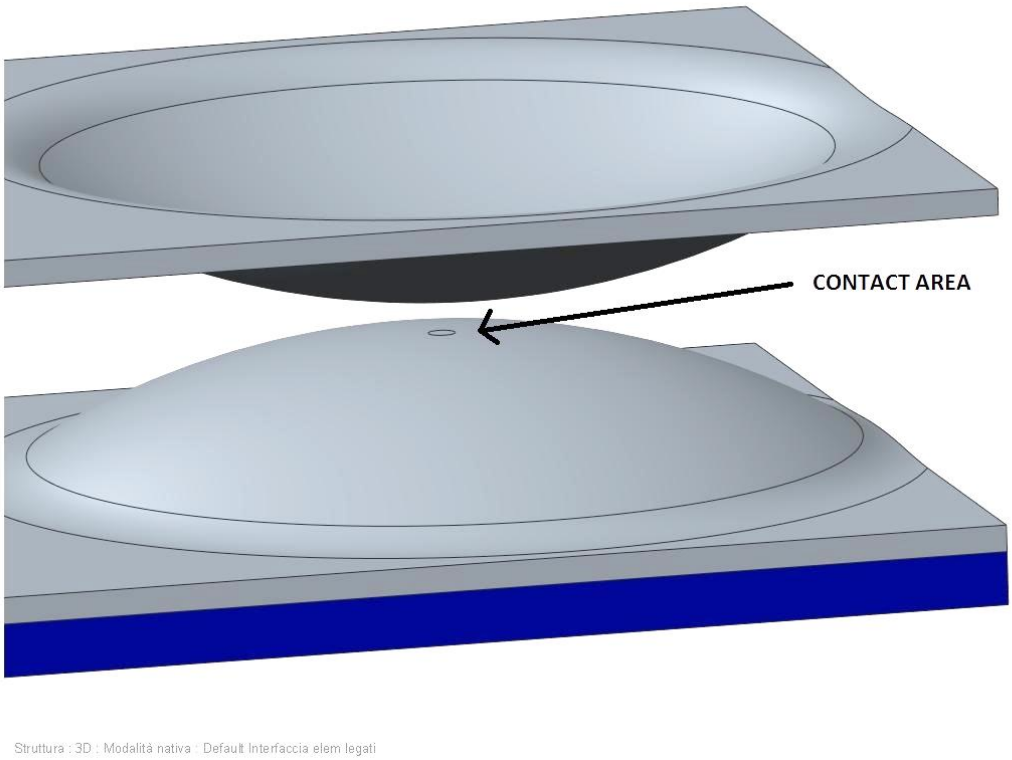

Figure 2-19. Detailed view of the crystal-support contact.

Two material models were used in the analysis. Quartz was assigned to the entire resonator disk, while stainless steel (AISI 316L) modeled the supports' material. Values are shown in the following table and are supported by previous literature (Scaccabarozzi, et al., 2014).

	QUARTZ	**AISI 316L**	***Unit***
Thermal Conductivity	6.2	14	*W/(m K)*

CTE	13.2	16	$\cdot 10^{-6}\ °C^{-1}$
Elastic modulus	97.2	193	*GPa*
Poisson's ratio	0.17	0.29	-

Table 2-5. Material properties.

Both materials were modeled with isotropic behavior. This is not an issue for the steel but is surely a strong approximation for quartz (section 1.3). The choice was motivated by the lack of information on the way the crystal disk was oriented with respect to the supports. Therefore, the values for quartz were chosen in such a way to reach the most critical condition possible that is the one with maximum stresses. For this reason, the highest CTE and elastic modulus were selected among the ones provided by literature, while the thermal conductivity was kept to the minimum value.

As for the mesh, 3D wedge elements were chosen. A finer mesh was created near the contact areas for the sake of accuracy.

2.4.2 Loads

The only load present was the one due to joule heating. The power given to the device was 0.464 W and it was localized in the heater area of the crystal. However, it would have been unrealistic to model the total load as uniformly distributed throughout the heater circuitry. It is in fact known that, given a certain current value, the heat released depends on the resistance, which ultimately depends on the area. Hence, the following steps were made in order to understand the actual distribution of heat on the crystal:

- The heater was split (in the model) in smaller areas with a rather simple geometry;
- Lengths and areas were measured (using the software);
- Resistances were computed according to the following formula:

$$R = \rho \frac{l}{A} \tag{2.19}$$

where l and A are respectively length and transversal area[15]; ρ is the resistivity.

[15] With respect to the current flow. Notice how this introduces the necessity of knowing the heater thickness.

- The power on each subpart was computed according to the Joule heating equation:

$$W = i^2 R \tag{2.20}$$

Figure 2-20 shows how the heater was split.

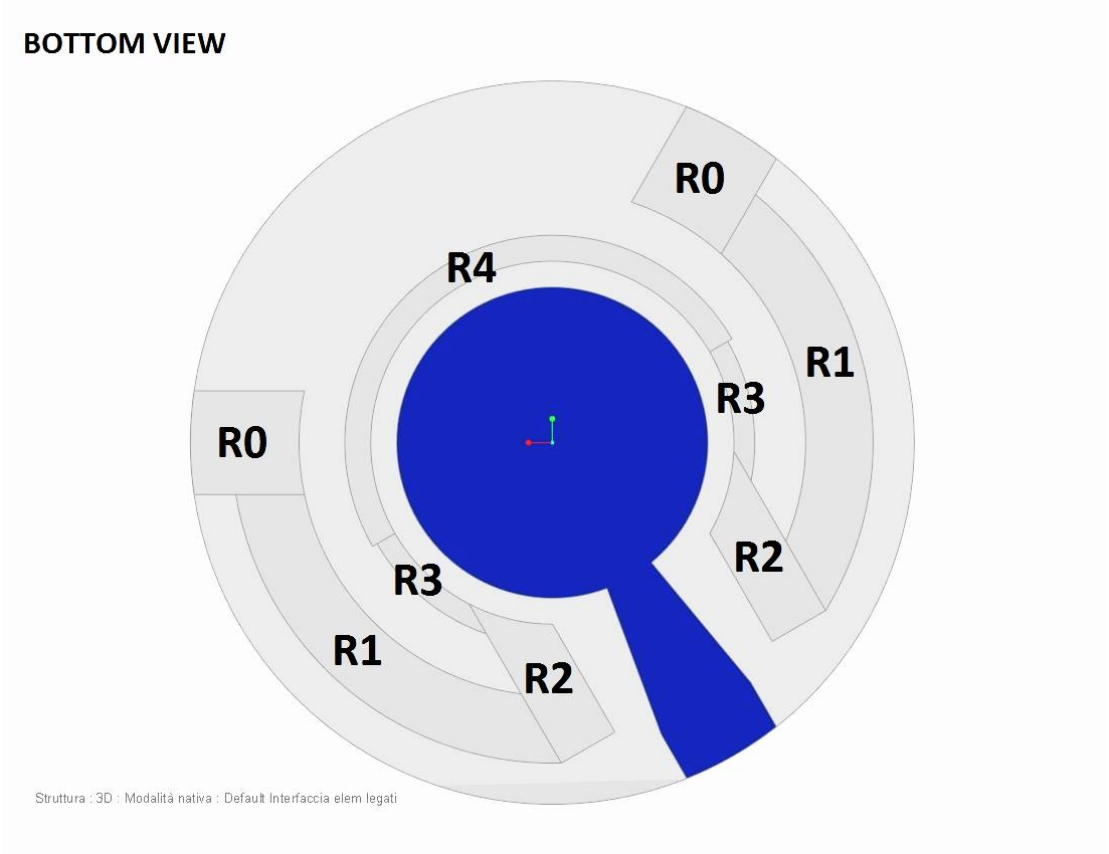

Figure 2-20. Heater subparts.

Due to the heater symmetry, it was necessary to make the above-mentioned calculations on only five out of the nine subparts.

The following table highlights the calculations made and the results obtained.

DATA	
RESISTIVITY *[Ω*m]*	6.40E-07
THICKNESS *[m]*	1.60E-07

CALCULATIONS

	R1	*R2*	*R3*	*R4*	*R0*
LENGTH *[m]*	7.47E-03	2.98E-03	2.39E-03	1.18E-02	2.12E-03
AREA *[m^2]*	2.29E-10	2.29E-10	8.51E-11	8.00E-11	3.22E-10
RESISTANCE *[Ω]*	2.08E+01	8.32E+00	1.80E+01	9.42E+01	4.22E+00
TOTAL RESISTANCE (Ohm)	1.97E+02				
CURRENT *[A]*	4.85E-02				
POWER *[W]*	4.90E-02	1.96E-02	4.23E-02	2.22E-01	9.92E-03
TOTAL POWER [W]	4.63E-01				

Table 2-6. Heat loads computations.

The heater resistivity was not exactly known. Earlier assumptions provided a value of $8.32 \cdot 10^{-7}$ Ωm but in cases very much different from the one in this thesis (Kulkarni, 1997). In fact, if the latter value were used, it would have been not possible to match the resistance and power requirements. Thus, the resistivity value was tuned to give total resistance and power as close as possible to the measured values of Table 2-4. The same order of magnitude was kept.

Results highlight that there is a good match in terms of total power. The total resistance, however, is slightly higher than the measured one. This is due to the approximated nature of heater's area measurements as well as the assumed resistivity value.

2.4.3 Constraints

Constraints introduced in the model were in the form of convection and radiation boundary conditions, as well as prescribed temperature values.

The convection constraint is expressed by the following linear equation

$$W = h_c A(T_W - t_\infty) \tag{2.21}$$

where h_c is the conduction coefficient, A is the surface area, while T_w and T_∞ are respectively the fluid working temperature and the environmental one[16]. W is the power delivered through the volume boundaries. All of the parameters are known except for h_c. Technical literature provides the details of its expression (IHS Global Ltd, 1978).

For a horizontal surface in air, the formula is the following:

$$h_{c,h} = C_1 \left(\frac{f\Delta T}{M}\right)^{1/4} \tag{2.22}$$

where ΔT is the difference of surface and environment temperatures (expressed in kelvin), f is the so-called relative pressure factor (equal to one since the test was performed in air), M is the area to perimeter ratio; C_1 is a constant and is given in tabular form. The latter in particular changes depending on which surface is considered. In fact, it is known that convective heat transfer is more effective on the microbalance's upper surface with respect to the bottom one. This is because the layer of heated air surrounding the microbalance, becomes less dense thus tends naturally to move upward; this is easier to happen on the upper face.
Note also that ΔT should be computed for each 'point' of the surface because of its non-uniform temperature distribution. However, calculations were made considering an average surface temperature (110 °C).

For a vertical rectangular surface in air, the formula is different:

$$h_{c,v} = \left[0.825 \sqrt{\frac{\lambda_f}{H}} + 0.605 \sqrt[6]{\frac{f\Delta T}{\lambda_f}} \right]^2 \tag{2.23}$$

[16] A more accurate definition would say that T_∞ is the temperature of air at a distance sufficient to consider null the effect of convective heat transfer.

where λ_f is the fluid mean conductivity[17] and H is the surface height.

In the FEM model, convection constraints were introduced on the microbalance top and bottom surfaces, as well as supports' horizontal and vertical ones. The latter are identified by the '*AISI'* subscript. Results from Eq. 2.22 and Eq. 2.23 as well as the data used are reported in the next two tables.

Data	Value	Unit
$t_{ave,crystal}$	110	$[°C]$
$t_{ave,AISI}$	50	$[°C]$
t_∞	22.7	$[°C]$
f	1	[-]
$C_{1,down}$	0.46	[-]
$C_{1,up}$	1.71	[-]
$M_{crystal}$	3.49E-03	$[m^2]$
M_{AISI}	1.36E-01	$[m^2]$
H	1.60E-03	$[m]$
λ_f	2.71E-02	$[W/(m\ K)]$

Table 2-7. Data for convection boundary conditions.

Coefficient	Value	Unit
$h_{c,h,crystal,up}$	15.00	$[W/(m^2K)]$
$h_{c,h,crystal,DOWN}$	5.79	$[W/(m^2K)]$
$h_{c,h,AISI}$	1.73	$[W/(m^2K)]$
$h_{c,v,AISI}$	28.00	$[W/(m^2K)]$

Table 2-8. Convection coefficients.

The radiation constraint is of the form of Eq. 2.24

$$W = \sigma \varepsilon A (T_w^4 - T_\infty^4) \tag{2.24}$$

with obvious meaning of the symbols.
It is known that the radiation condition makes the model non-linear, thus slows down the whole computation. Moreover, both radiation and convection constraints must be

[17] That is, the conductivity measured at a temperature of $\frac{T_w+T_\infty}{2}$ °C. Data is easily found in technical literature, for instance at https//:www.engineeringtoolbox.com

applied to the same surfaces and the software allowed only one condition for each surface to be set. For this reasons, the radiation constraint was linearized. The procedure is based on the reduction of a difference of two squared quantities[18]. Thus, Eq. 2.24 becomes

$$W = h_r A(T_w - T_\infty) \tag{2.25}$$

and h_r is the linearized radiation coefficient, given by the following expression

$$h_r = \sigma\varepsilon(T_w^2 + T_\infty^2)(T_w + T_\infty) \tag{2.26}$$

Apart from the dependence on temperature (once again, average ones were considered), the coefficient depends on the emissivity. This means that h_r assumes a different value corresponding to the different emitting materials. In particular, the radiation from the supports was neglected since the latter are plated with gold and have a very low emissivity.
The temperature used in the calculations are the one in Table 2-7 and the emissivity values were previously discussed (Table 2-2). The computed coefficient are shown in the next table. It is interesting to note that convective and radiation coefficients are of the same order of magnitude.

Coefficient	Value	Unit
$h_{r,crystal}$	6.00	$[W/(m^2K)]$
$h_{r,heater}$	2.71	$[W/(m^2K)]$
$h_{r,electrode}$	2.48	$[W/(m^2K)]$

Table 2-9. Linearized radiation coefficients.

In conclusion, a properly defined sum of convective and linearized radiation coefficients was assigned to each of the microbalance's surfaces.

Finally, temperature was prescribed in the supports' bases. The value assigned was 22.7 °C in order to impose ambient temperature condition sufficiently far from the crystal. This fact was also verified during testing: these parts showed no sign of heating.

[18] In fact, $(a^4 - b^4) = (a^2 - b^2)(a^2 + b^2)$ which ultimately yields $(a - b)(a + b)(a^2 + b^2)$.

2.4.4 Results

A measure of the *maximum* z-directed[19] thermal gradient on the microbalance was performed during simulation. Figure 2-21 illustrates the result.

Measures:

Name	Value	Convergence
energy_norm:	2.038795e+04	0.0%
max_flux_mag:	1.763743e+04	3.3%
max_flux_x:	1.420911e+04	13.6%
max_flux_y:	1.417433e+04	15.2%
max_flux_z:	-1.091691e+04	10.9%
max_grad_mag:	2.653136e+03	15.6%
max_grad_x:	1.937765e+03	12.9%
max_grad_y:	-2.286182e+03	15.2%
max_grad_z:	1.375854e+03	15.4%
max_temperature:	1.170263e+02	0.0%
min_temperature:	2.266739e+01	0.0%
Grad_Z:	-2.432527e-01	0.0%

Analysis "test_prova_EQConv" Completed (11:08:30)

Figure 2-21. Gradient measure after thermal analysis.

It can be seen that the value converges with a high accuracy to -0.24 °C/mm. Since the microbalance is 0.167 mm thick, the maximum temperature difference between the top and bottom surfaces can be estimated at around 0.04 °C. This quantity is very small, thus it can be concluded that the hypothesis of negligible thermal gradient in the thickness direction was verified.

The convergence of the overall analysis was checked. The global energy norm reaches a steady value after increasing the shape functions' order up to five (Figure 2-22). This means that the result approaches the unique model solution. Moreover, no singularities nor warnings were evidenced.

[19] Z-axis is orthogonal with respect to the microbalance's surfaces.

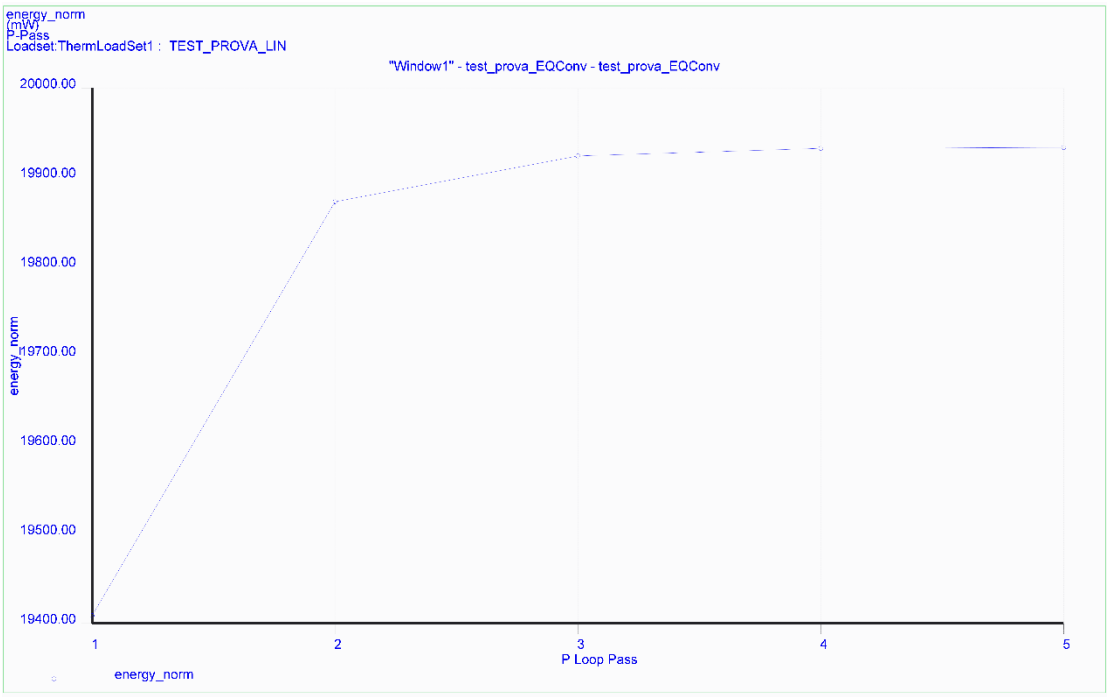

Figure 2-22. Converge plot of FEM model.

Then, the thermal field extracted from the FEM analysis was compared with the one of the experiment (Figure 2-16). In order to do so, seven portions of the crystal surface were identified in correspondence to the quartz crystal. All the other areas were unreliable sources of temperature information because of the high uncertainty value.
Figure 2-23 highlights all the visible crystal areas used for the thermal field comparison.

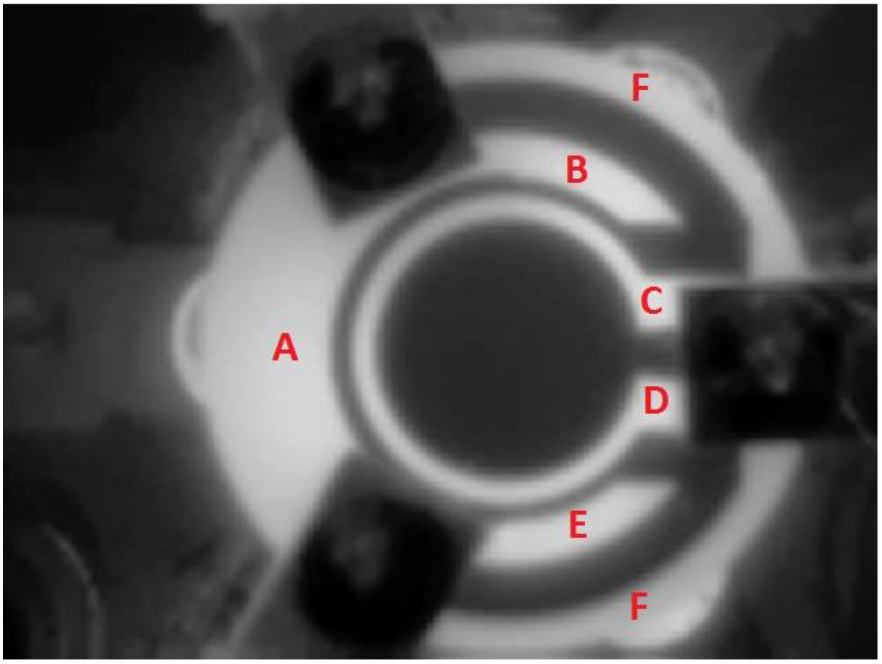

Figure 2-23. Visible crystal areas.

With the help of the code of ANNEX D, maximum and average temperature were computed for each area and then compared with the respective quantities in the model. The following tables show the obtained results.

PART	$T_{ave,test}$ [°C]	$T_{ave,model}$ [°C]	$T_{max,test}$ [°C]	$T_{max,model}$ [°C]
A	110 ± 4	108.2	116 ± 4.6	113.4
B	112 ± 4.5	112.8	116 ± 4.6	113.6
C	116 ± 4.6	112.2	116 ± 4.6	113.4
D	116 ± 4.6	113.1	114 ± 4.6	113.9
E	111 ± 4.4	108.7	112 ± 4.5	110.6
F	100 ± 4	100.7	104 ± 4.1	103.9

Table 2-10. Results comparison on first trial.

PART #	$Error_{ave,temp}$ [°C]	$Error_{max,temp}$ [°C]
A	1.8	2.6
B	-0.8	2.4
C	3.8	2.6
D	2.9	0.1

E	2.3	1.4
F	-0.7	0.1

Table 2-11. Errors on first trial.

It can be seen that the values are quite close but given the approximated nature of the convective coefficients used in the model, there is room for improvement. For this reason, the above-mentioned coefficients were tuned with a trial and error approach in order to fit the experimental data better.

After many different trial processes, the optimum result was achieved (Table 2-12).

PART	$T_{ave,test}$ [°C]	$T_{ave,model}$ [°C]	$T_{max,test}$ [°C]	$T_{max,model}$ [°C]
A	110 ± 4	110.1	116 ± 4.6	115.2
B	112 ± 4.5	112.7	116 ± 4.6	116
C	116 ± 4.6	115.4	116 ± 4.6	115.4
D	116 ± 4.6	115.9	114 ± 4.6	112.9
E	111 ± 4.4	110.3	112 ± 4.5	111.6
F	100 ± 4	100.4	105 ± 4.1	106

Table 2-12. Results comparison with optimized model.

PART #	$Error_{ave,temp}$ [°C]	$Error_{max,temp}$ [°C]
A	-0.1	0.8
B	-0.7	0.0
C	0.6	0.6
D	0.1	1.1
E	0.7	0.4
F	-0.4	-1

Table 2-13. Error with optimized model.

It can be seen that the maximum error on the average temperature is 0.7 °C (it was previously equal to 3.8 °C), while the one on the maximum temperature is 1.1 °C (lower than the 2.6 °C of Figure 2-11).

The optimum condition was reached using the following coefficients.

Coefficient	Value	Unit
$h_{r,crystal}$	6.00	$[W/(m^2K)]$
$h_{r,heater}$	2.71	$[W/(m^2K)]$

$h_{r,electrode}$	2.00	$[W/(m^2K)]$
$h_{c,h,crystal,UP}$	15.00	$[W/(m^2K)]$
$h_{c,h,crystal,DOWN}$	5.79	$[W/(m^2K)]$
$h_{c,h,AISI}$	1.73	$[W/(m^2K)]$
$h_{c,v,AISI}$	28.00	$[W/(m^2K)]$

Table 2-14. Optimized coefficients.

The thermal field extracted is shown in the following figures.

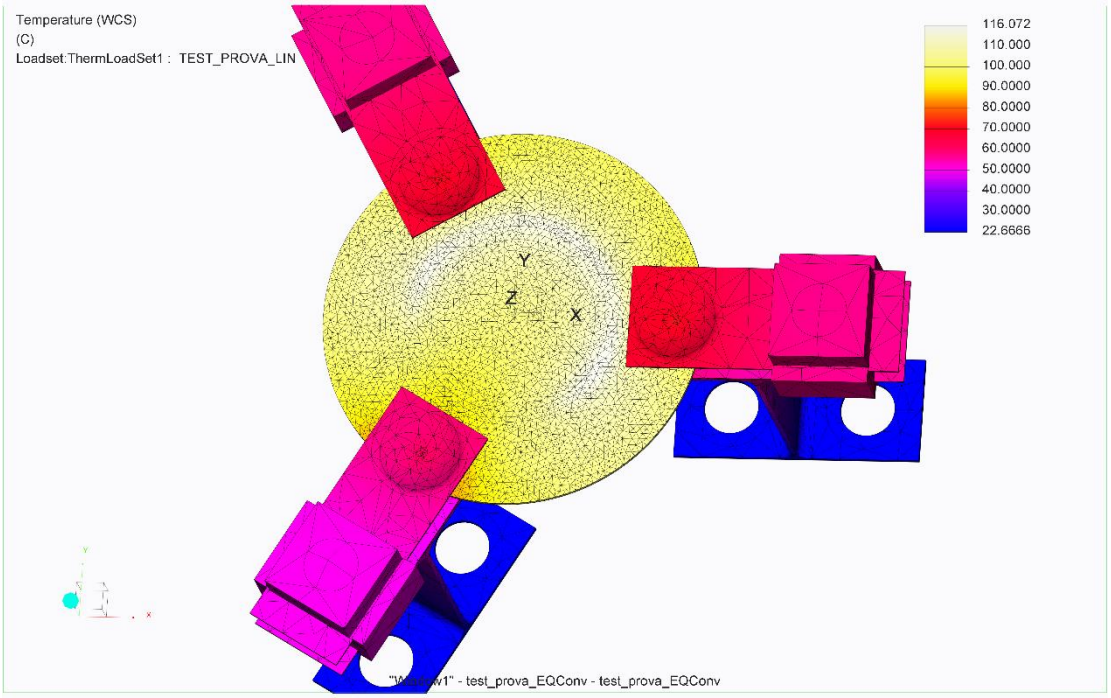

Figure 2-24. Thermal field on entire microbalance.

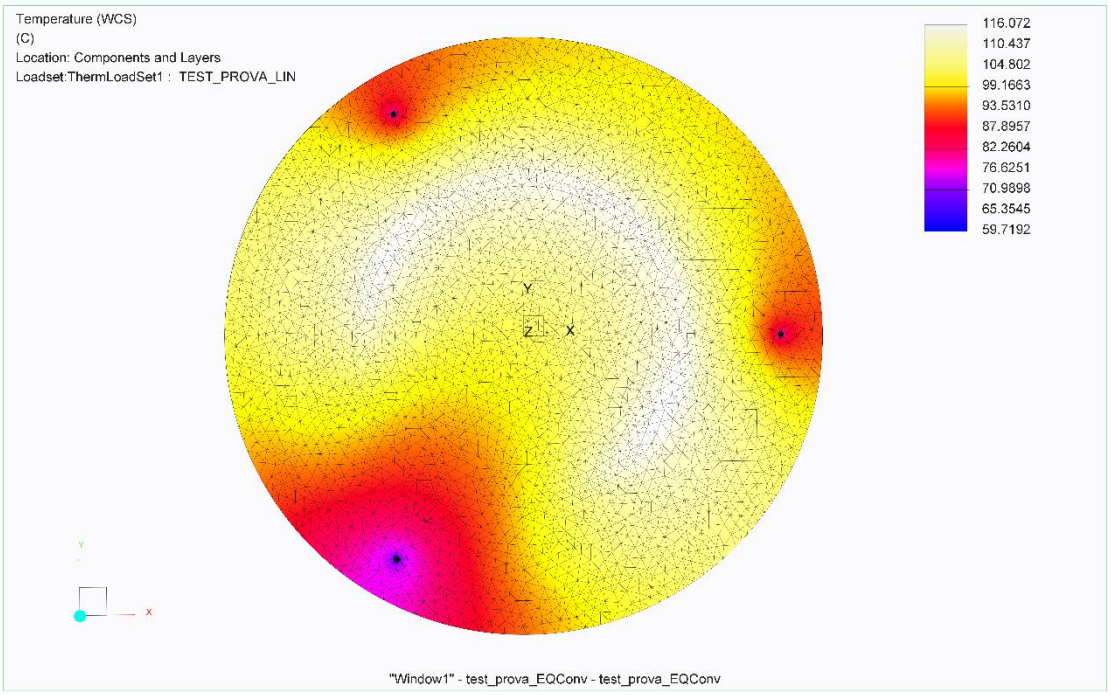

Figure 2-25. Thermal field on disk only.

The thermal field is symmetric with respect to an axis passing through the center of the disk surface and rotated of 60° from the X-axis. Moreover, only the crystal's upper surface is shown in Figure 2-25 because of the negligible gradient along the thickness. It can be noted that the areas of highest temperature are the ones of the heater. This is expected since those areas receive a direct heat load. The supports' bases have the lowest temperature value, which is the prescribed one (22.7 °C).
Concerning the crystal, the lowest temperature is of around 60 °C. This value is reached on the regions of contact with the three supports where heat is dissipated through conduction. Considering also that steel has a higher thermal conductivity (more than twice the value for crystal) this phenomenon is soon explained.

A structural analysis was then conducted by using the computed thermal field as a load. The clamping pre-loads previously discussed were considered as well. A boundary condition was imposed to prescribe all the displacements on the supports' bases. This is consistent with the fact that the microbalance is fixed on a basement by means of bolts (Figure 1-8).
The mesh used for the previous analysis was kept.
As mentioned earlier, the worst condition possible in terms of stresses was under investigation (maximum CTE and elastic modulus).

Convergence of the FEM model was checked with positive outcome.

The following figure illustrates how the structure deforms (Figure 2-26).

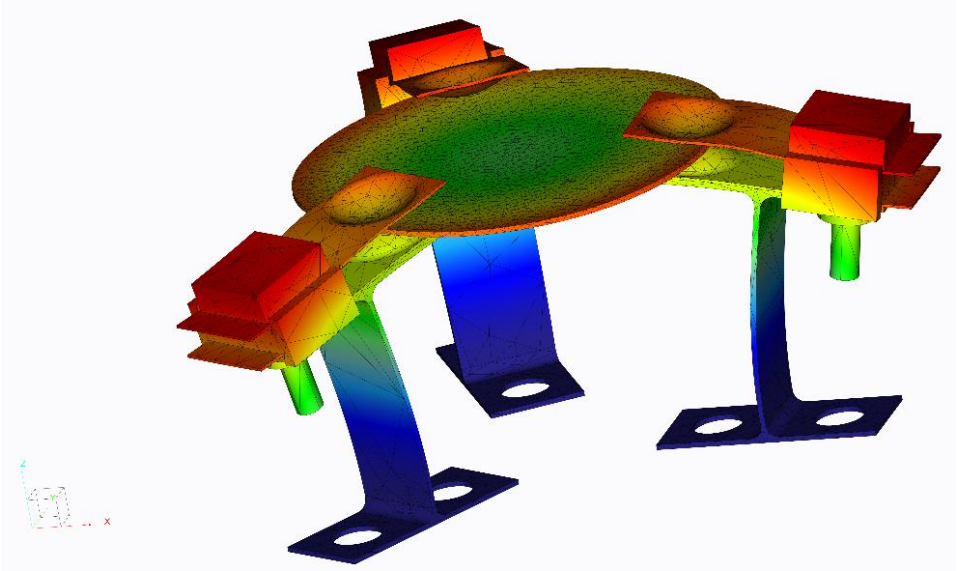

Figure 2-26. Microbalance deformed shape.

The deformed shape is consistent with what expected. In fact, the expansion of the quartz crystal makes the supports bend with the result that the crystal is moved upwards.

Figure 2-27 displays the crystal orthogonal displacements (Z-axis). It can be seen that the central part of the disk lays at the bottom. This shape is consistent with preliminary tests with oil. Displacements are of thousandths of millimeter order of magnitude and the red areas are $95 \cdot 10^{-4}$ mm above the blue ones.

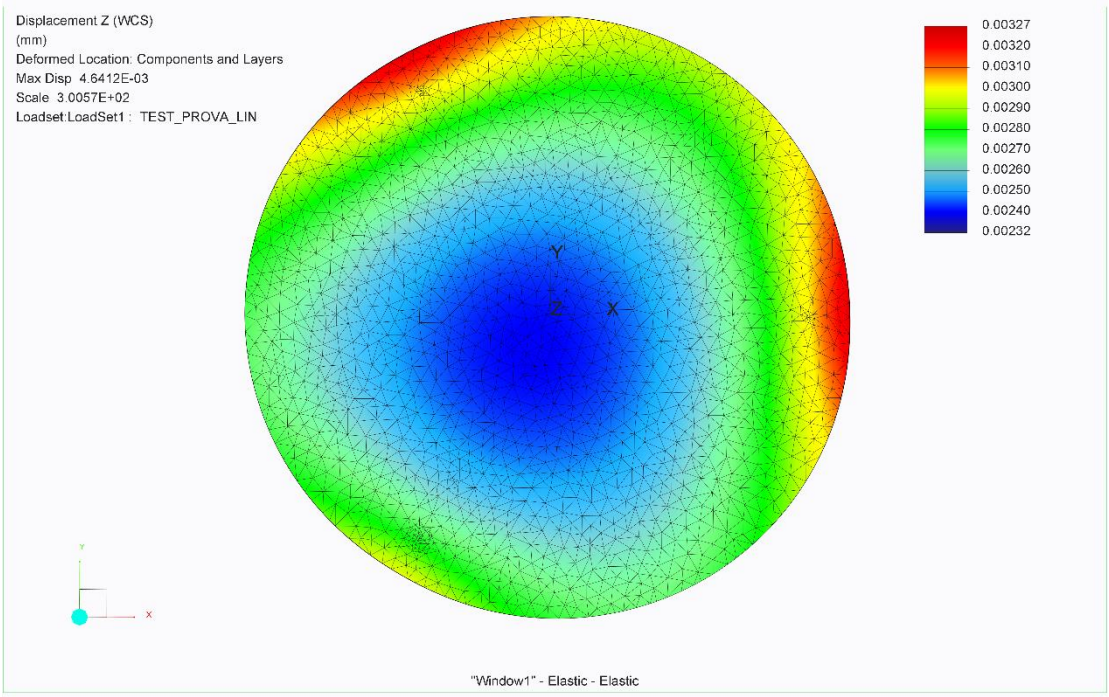

Figure 2-27. Crystal's orthogonal displacements.

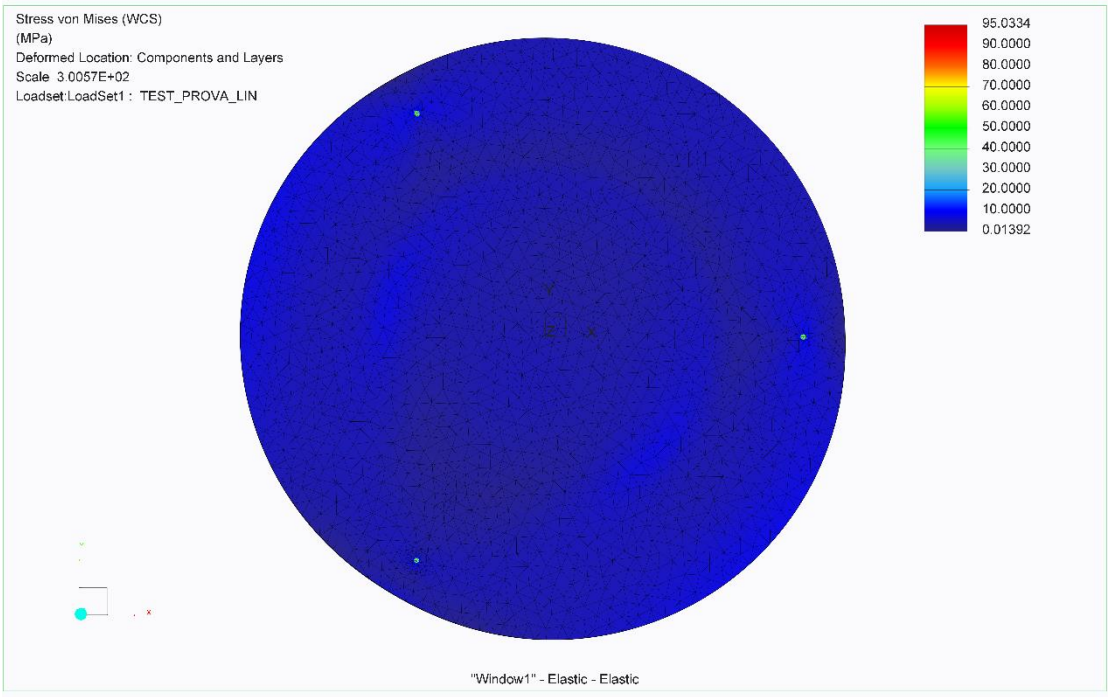

Figure 2-28. Stress on the crystal.

Figure 2-28 highlights the stress values on the crystal. The regions where the pick value of 95 MPa is reached are the three areas of contact with the supports. On the rest of the crystal, the Von Mises stress never exceeds 5.8 MPa.
Considering that in the worst scenario yielding occurs at 41 MPa, the stress value on the contact areas is too high. However, this is a spurious result. In fact, the model over-constrained those areas by imposing a rigid link between crystal and supports. In practice, this is not what happens because of the different CTE of quartz and steel, i.e. some certain amount of sliding might take place. Moreover, the many experimental tests carried out before the start of this work did not evidence failure, nor crack propagation, even at temperatures much higher than the ones on this work. Hence, it is empirically known that the device is safe.
Thus, what engineering judgment suggests is that the maximum stress value is due the model simplification rather than being the real one. Clearly, the work highlighted the need for a more in-depth investigation on this topic.

The maximum Von Mises stress on the supports is around 5 MPa. The yielding stress for the steel used is of 235 MPa, thus the safety condition is satisfied.

CHAPTER 3

This chapter deals with the thickness shear modes (TSM) of the quartz disk. First, general results are presented concerning the TSM frequency. The disk model is validated at ambient temperature. Then, the discussion goes deeper in the important topic of temperature effects on the vibration frequency. More specifically, uniform and non-uniform temperature fields are introduced in the analysis. Results are discussed.

3.1 FEM model for TSM analysis

The FEM model used in this section is shown in the following figure.

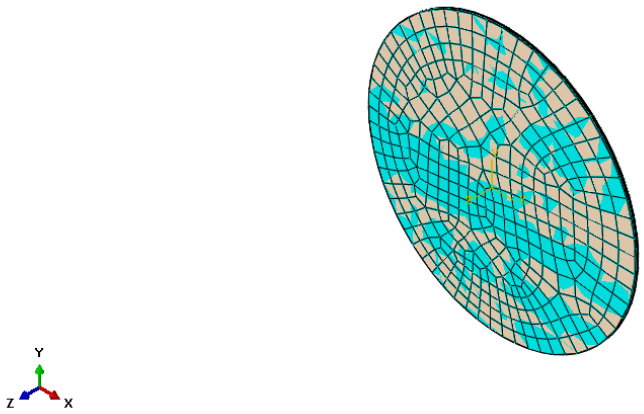

Figure 3-1. FEM model for modal analyses.

Only the crystal was modeled because this is where TSM takes place[20].

Electrodes were, once again, not included. This time the choice was motivated by the fact that an electrode, like the one of the microbalance under study, changes the TSM

[20] It can be noted that symmetry could have been exploited by modelling only a quarter of the disk. In addition, a 2D model was an option considered before continuing the study. However, a 3D model was chosen because the original idea was to import the temperature field of the previous analysis, which was in 3D. Eventually, this was not done because of the problems encountered as will be pointed out later on in this chapter.

frequency of only two parts by 10^7 Hz (Hewlett Packard, 1997). With a similar reasoning, it was decided not to model the heater as well.

Concerning the mesh, 3D 8-node elements were chosen. Particular attention was dedicated to the discretization of the crystal thickness because the model must allow a shape like the one previously shown in Figure 1-2. On the other hand, it is known that a high number of nodes on the surfaces does not affect the extraction of the shear frequency. Because of these considerations, a bottom-up approach was used for the meshing technique. In other words, the mesh was created on the top surface. Then, it was propagated to the other one, specifying how many layers were needed in-between.

Displacements orthogonal to the planar surfaces were prevented on all crystal's boundaries. This was done in order to speed-up the analysis by avoiding the extraction of flexural and spurious modes that are outside the scope of the analysis.

As for the material properties, the ones used in the previous chapter were found to be inappropriate for the modal analysis. This is because the elastic modulus value was chosen regardless of the AT-cut orientation. This implied a non-negligible error in the resulting frequency value. Moreover, the isotropic model provided the result that two vibrating modes (orthogonal to each other) happened at the same frequency value. This fact clearly contradicts what known from literature. Further details on this topic can be found in ANNEX E.

Thus, the anisotropic behavior of quartz was introduced in the model. Since the supports were excluded from the analysis, it was possible to use the elastic coefficients shown in section 1.3 with no orientation restriction[21]. The elastic matrix is here reported for simplicity.

$$[E] = \begin{bmatrix} 87.49 & 27.07 & -8.93 & 3.36 & 0 & 0 \\ 27.07 & 102.84 & -7.34 & -9.89 & 0 & 0 \\ -8.93 & -7.34 & 130.36 & -5.44 & 0 & 0 \\ 3.36 & -9.89 & -5.44 & 38.73 & 0 & 0 \\ 0 & 0 & 0 & 0 & 29.36 & -2.14 \\ 0 & 0 & 0 & 0 & -2.14 & 69.25 \end{bmatrix} \quad (1.8)$$

[21] X and Y axes could be placed arbitrarily on the disk surfaces since this fact does not alter the frequency value. In fact, if those axes were switched, the same eigenvalues would be extracted but with a differently oriented mode shape. On the other hand, Z axis is always orthogonal to the disk surfaces.

It can be seen that there are three different shear moduli associated with this material (the last three values on the main diagonal). Among them, the highest one is torsional (Bechmann, et al., 1962) and the other two (respectively 29.36 and 38.73 GPa) are the ones responsible for TSM. The fact that there are two different thickness shear modes with displacements orthogonal to each other is confirmed by literature (Vig, 2004).
In this study, the lower of the two TSM frequencies was considered. Anyway, the discussion can easily be extended to the other one.

Another point worth to be mentioned is that damping was excluded from the model. The crystal has a high Q factor (see section 1.2). This means that the damping ratio is very small and, for this reason, its effects were neglected in the analysis.

As mentioned in the introduction, theory of elasticity can be used to estimate the frequency at which TSM takes place. By introducing the value of 29.36 GPa in Eq. 1.3, the latter yields a result of 9.97 MHz. In similar fashion, the experimentally deduced Eq. 1.4 indicates a frequency of 9.94 MHz, a value very similar to theoretical one. Technical literature offers even more support to this value (Wudy, et al., 2009).
It is worth to be noted that, since the FEM result is extensively confirmed by theory, the change of base performed on quartz's elastic matrix (section 1.3) was also validated.

The resulting mode shape is displayed in the following two figures[22].

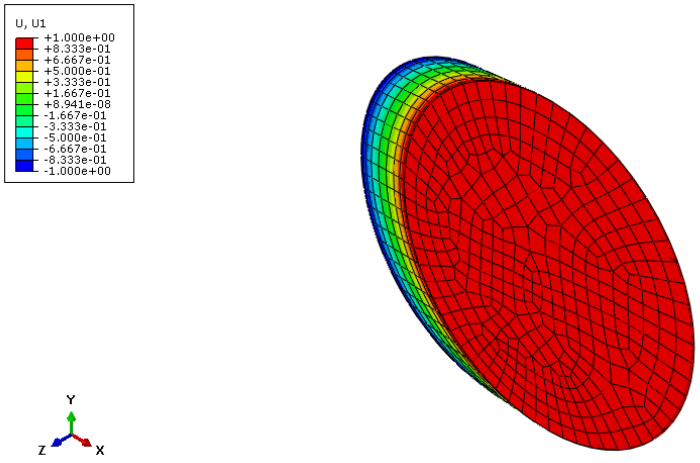

Figure 3-2. Modal shape.

[22] Images shown are taken from the analysis with nine thickness elements.

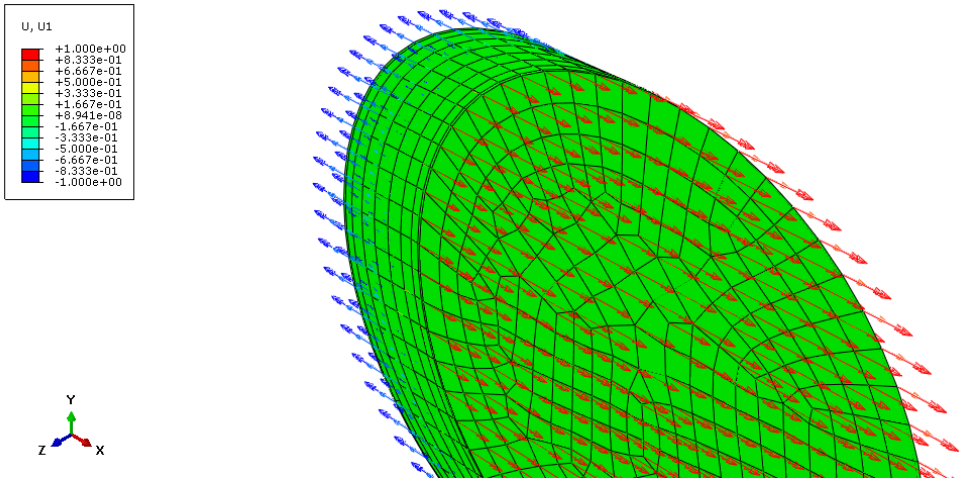

Figure 3-3. Nodal displacement vectors.

As expected, top and bottom surfaces slide parallel to each other, in opposite direction and of the same quantity. This is confirmed by the nodal displacement vectors of Figure 3-3 and by the color grid in Figure 3-2. Moreover, since the shear modulus used was the one on the Y-direction, TSM happens in the X-direction accordingly.

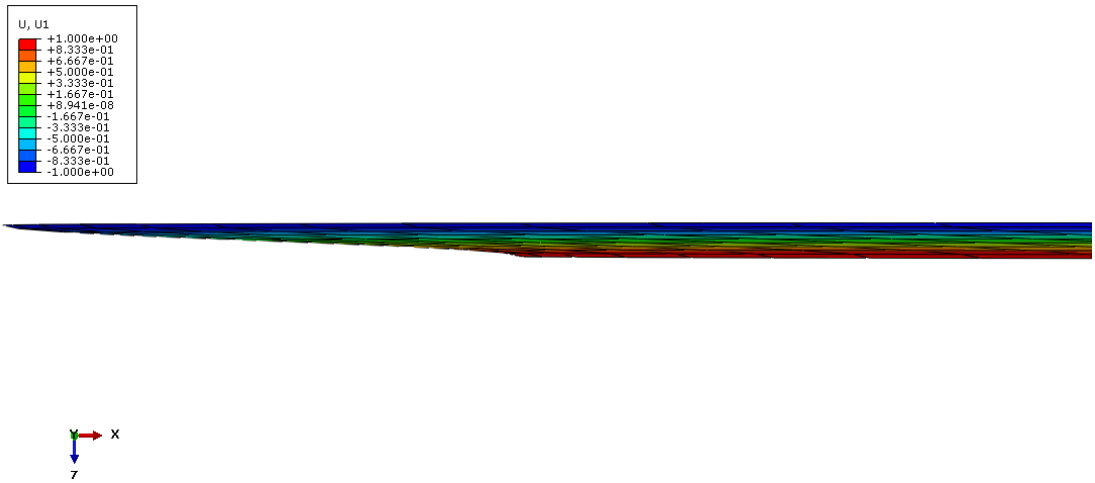

Figure 3-4. Deformed shape along thickness.

Figure 3-4 shows that the deformed shape along thickness is coherent with the theoretical one discussed in the introduction and shown in Figure 1-2.

As for the frequency value, Figure 3-5 confirms that it converges to 9.93 MHz as the number of thickness elements is increased. This is coherent with theory.

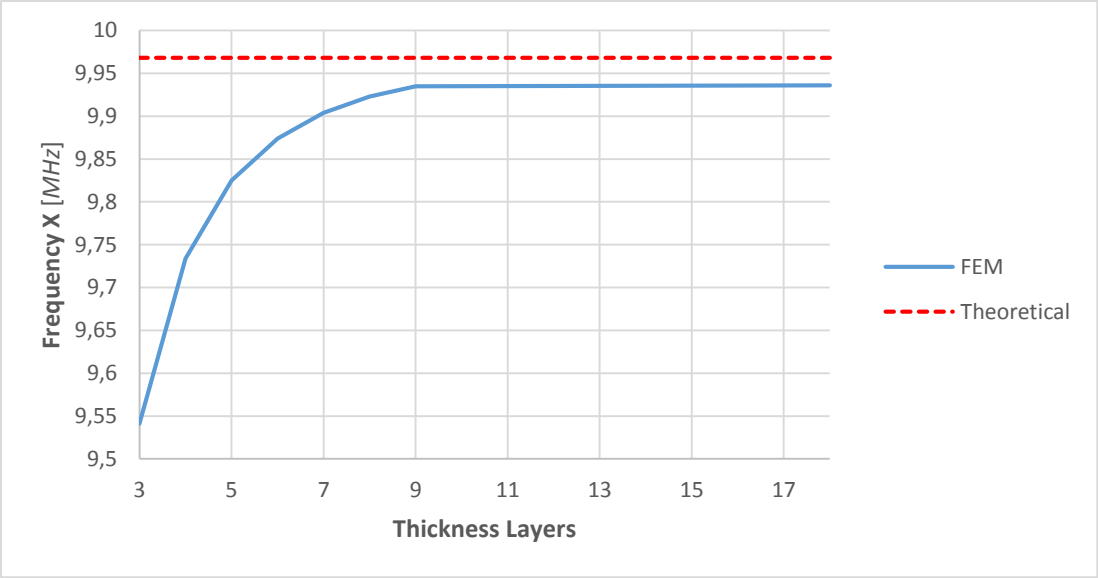

Figure 3-5. Modal analysis results.

Even the actual microbalance's TSM frequency was found to be around 10 MHz. However, the values experimentally measured are slightly scattered. This happens because the real device differs from the model (and theoretical concepts) in many ways. For example, supports, electrodes and heater all play a role in determining the TSM frequency by creating localized variations of thickness (Eq. 1.3) and by increasing the microbalance's mass. Moreover, the actual device frequency of vibration is affected piezoelectricity, whose effects are excluded from both theory and FEM.

Therefore, it can be concluded that the model is validated for ambient temperature condition. In the following phase, the effects of temperature on the natural frequency were analyzed with particular attention to thermal gradients.

3.2 Frequency vs. Temperature

The effects of temperature on the microbalance were previously discussed form a wide perspective (section 1.2). However, it is important to remind that thermal gradients arise because of the microbalance's innovative built-in heater. Moreover, since the majority of the microbalances are heated in a furnace, the topic of thermal gradients in resonator devices has not been object of extensive research. This is the reason why little to no information was provided about this topic in the introductory part of the thesis.

Anyway, as mentioned earlier, the goal of this section is to shed light on the effects of a non-uniform thermal field on the thickness shear modes. The technique used was FEM.

First thing done was to check the model behavior under a constant temperature distribution. This served as a model validation.

A uniform temperature field was introduced in the model by properly varying the material parameters that determine the frequency behavior. From Eq. 1.3 it is known that they are density, elastic coefficients and thickness (or, equivalently, CTE[23]).
As mentioned in the introduction, technical literature provided tables with parameters-temperature values. Linear interpolation was performed between the provided values. This fact has very important consequences, which will be later discussed.

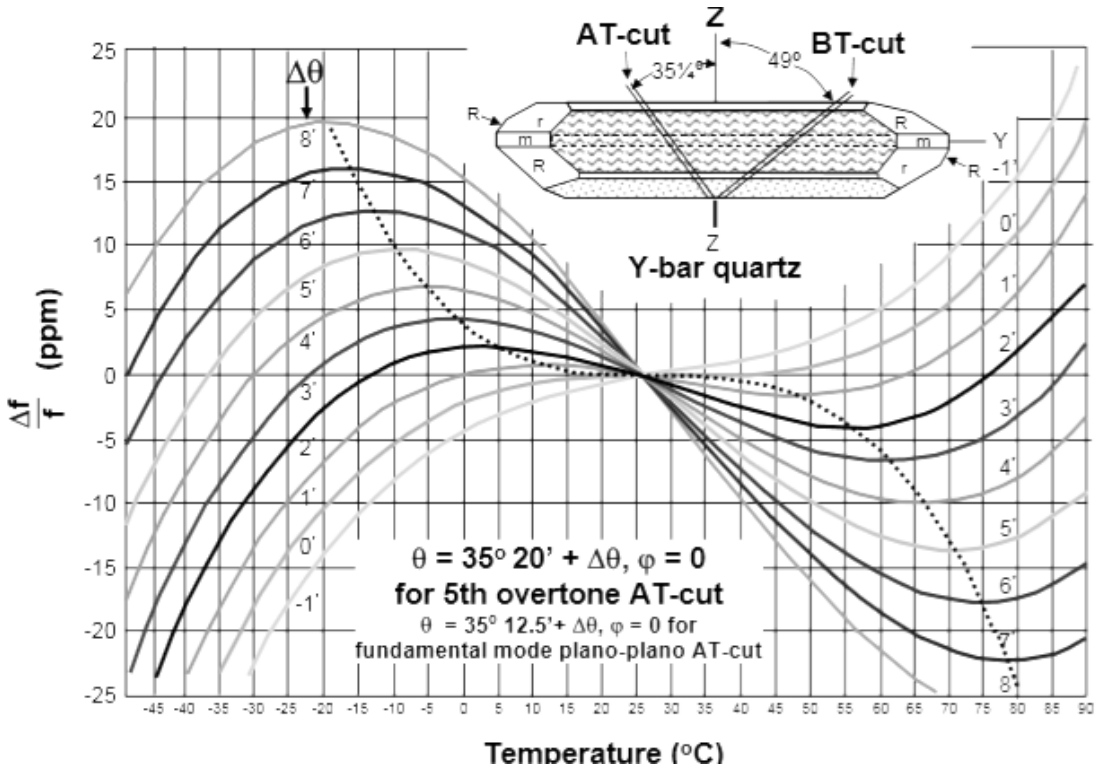

Figure 3-6. Example of the frequency-temperature curve with different cut angles (Vig, 2004).

[23] In fact, only the thickness variation is important for the analysis. The effects of CTE on the X and Y directions are not of interest.

Figure 3-6 shows an example of frequency-temperature behavior of an AT-cut quartz crystal. Since the Y-axis values are in ppm, frequency shifts are very small compared to the initial resonant frequency (around 10 MHz in the case under study). For example, a 1 ppm shift corresponds to a variation of the initial frequency of 10 Hz, which ultimately translates into a change in the last two figures of the 10 MHz number. Such a small variation can be difficult to be accurately detected by FEM technique since the latter is prone to numerical faults. For this reason, before starting the analyses, the software was set to work with double precision numbers in every step of the calculations made. Moreover, a finer mesh with respect to what previously shown, was used for the occasion. However, even if these preventative measures were adopted, a high accuracy on the results is not guaranteed *a priori*.

It should also be noted that the curves in Figure 3-6 are plotted for different values of the angle of cut. All other variables are kept constant. In this work, a pure AT-cut is under study and this means that ϑ is equal to 35° 15'. Therefore, it is not possible to compare the curve obtained by means of FEM with the one of Figure 3-6. However, from a qualitative point of view, it can be concluded that the frequency shift should increase with temperature. Moreover, it is known from theory that the curve should be close to a third degree polynomial (Hewlett Packard, 1997).

Figure 3-7 highlights the curve obtained from FEM.

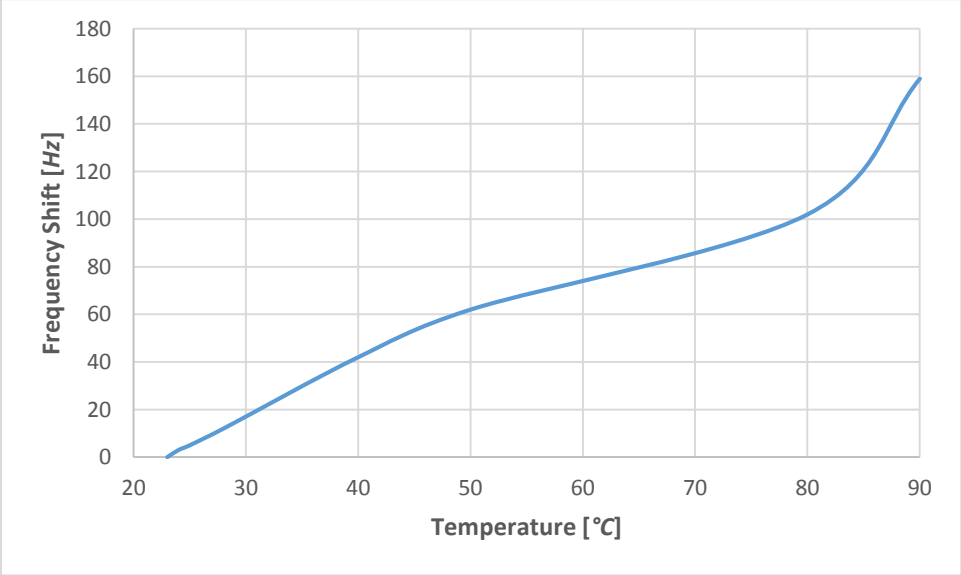

Figure 3-7. Frequency-temperature plot resulting from FEM analyses.

It can be seen that, while the FEM is able to catch qualitatively the increase in frequency shifts with temperature, the curve is not a third degree polynomial. The reason for this behavior lays in the approximated nature of the input parameters.
As mentioned earlier, the frequency-temperature curve is (in first approximation) the result of the combined effect of density, elastic coefficients and thickness variations. Eq. 1.3 is here reported for simplicity.

$$f_n = \frac{1}{2h}\sqrt{\frac{C_{ij}}{\rho}} \tag{1.3}$$

It is clear that, in order to get the exact frequency temperature behavior of Figure 3-6, the parameters in the equation (and in the FEM model) must be known with a high accuracy. In practice, they are not. First, they are experimentally determined and, therefore, a certain extent of uncertainty in their measurements is present. Second, their relation with temperature is not known in closed form but through a grid of points. Linear interpolation was used between the intermediate values and this is a strong source of error.

An estimate of the uncertainty on the frequency shift can be computed by using the propagation of uncertainties method already presented in chapter two. The absolute uncertainties of the three parameters can be estimated at respectively $0.005/\sqrt{3}$ GPa, $0.5/\sqrt{3}$ kg/m^3 and $0.005/\sqrt{3}\cdot10^{-6}$ m. In such a configuration, the uncertainty on the frequency shift was estimated at around 500 Hz.
The discussion can be summarized as follows. The model has a high sensitivity to the input parameters, and, since the latter are not known with enough accuracy, it is virtually impossible to get exactly a third degree polynomial out of the FEM modal analysis.

Previous tests showed that the frequency-temperature behavior of the crystal under study is as shown in the next figure (Longobardo, et al., 2015).

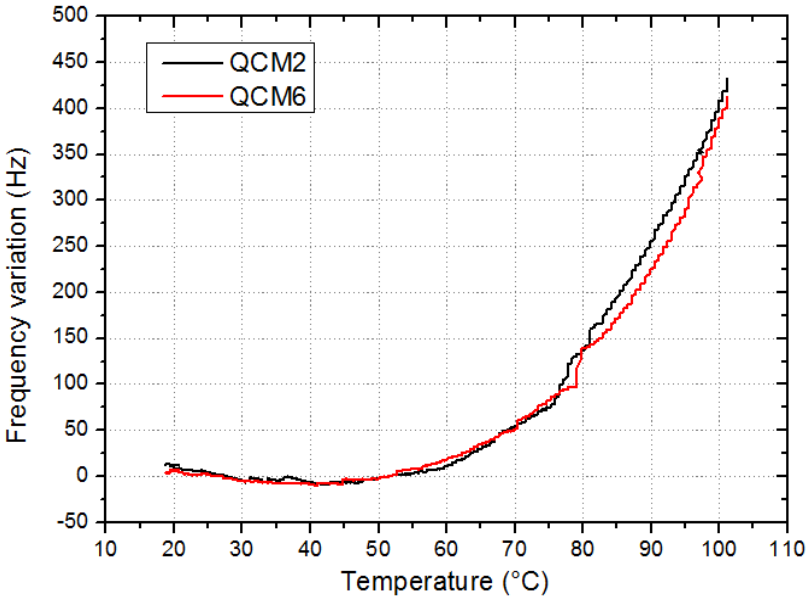

Figure 3-8. Frequency-temperature plot for crystal under investigation.

Each point of Figure 3-8 was obtained in steady state condition and under a homogeneous temperature field (thermal energy was not delivered from the heater). It can be seen that the crystal shows very small frequency shifts up to 50 °C; this phenomenon is also referred to as *temperature compensation*. Above this temperature, the curve behaves like a third order polynomial as expected.
The way this kind of crystals are manufactured is by either contouring or angle-correction techniques (Vig, 2004). The basic idea is that a quartz slab is tested in a trial and error process in order to find small corrections of the angle of cut and/or the thickness with the goal of having a frequency-temperature curve like the one in Figure 3-8. Due to high number of variables involved, the process is repeated for each single quartz slab. The consequence of interest for this thesis is that not even the angle of cut is known with precision. Clearly, this is another source of error.

A comparison of the curve resulting from FEM and the experimental one is shown in the next figure.

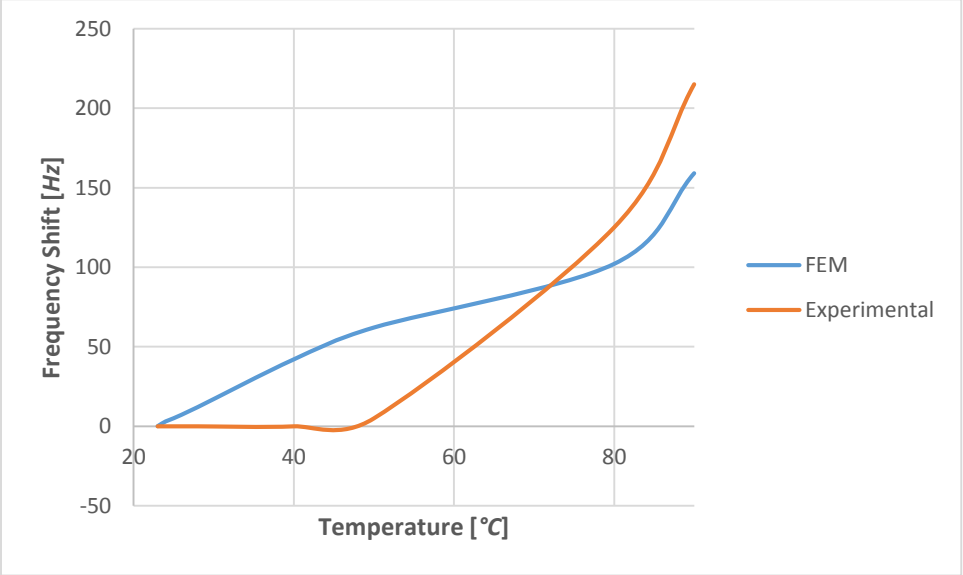

Figure 3-9. Comparison of FEM curve and experimental one.

It can be seen that the maximum difference is of around 60 Hz at 50 °C. Thus, it is concluded that the FEM errs of maximum 60 Hz.

For the sake of completeness, the FEM capability of reproducing the experimental behavior was tested. This served as a further proof of the claim that the FEM inaccuracies are due the input parameters. To do so, density and the elastic matrix were assumed as precisely known. The thickness was instead computed inverting Eq. 1.3 with the goal of matching the curve of Figure 3-8. The obtained curve is shown in the next figure.

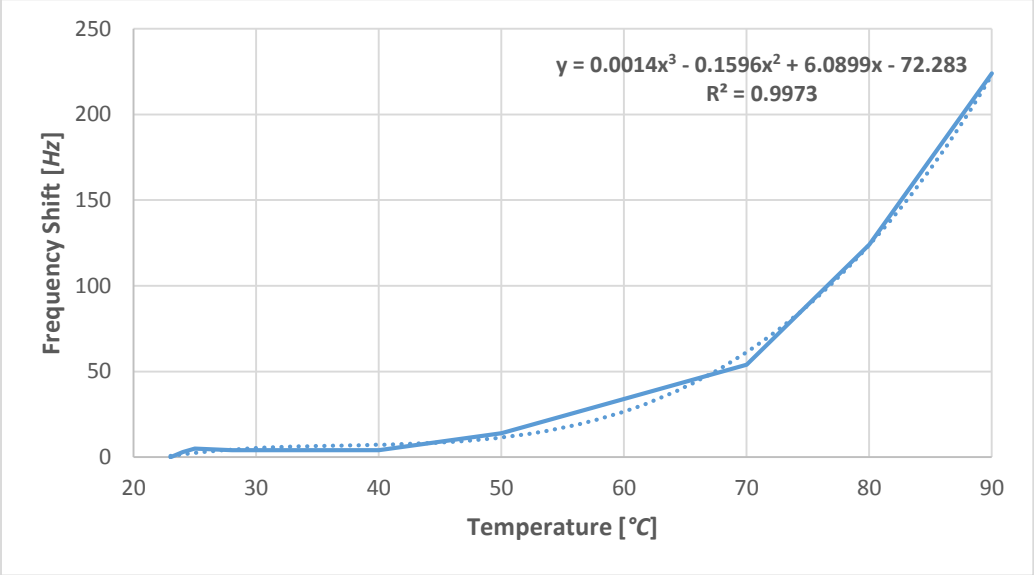

Figure 3-10. Ideal FEM result.

It can be seen that the curve is very close to the experimental one. The shape is also very well approximated by a third degree polynomial. However, the CTE used in these analyses showed a trend with temperature that is not consistent with what found in literature. This is because the thickness value had to compensate for the errors present in all the other parameters. This was too much of a forcing to be used in this study.
Yet this discussion clearly proves that it would be possible in theory to model the frequency-temperature behavior exactly as expected. However, this is prevented by the errors in the input parameters. The latter are entirely responsible for it. The FEM inaccuracies are not.

After this discussion, it becomes clear why the original idea of using the temperature field extracted from the static analysis was abandoned. This is because the model did not reproduce the actual microbalance well. For this reason, the attention was shifted towards the effects of a simpler, yet interesting, temperature gradient. The idea is highlighted in Figure 3-11.

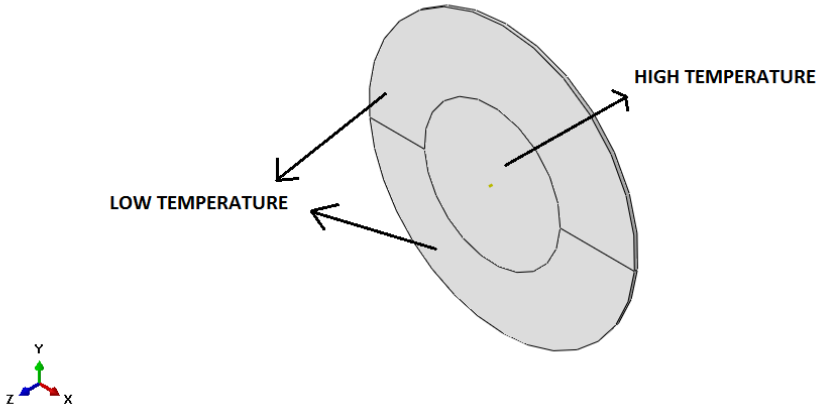

Figure 3-11. Model for thermal gradient study.

The original model was partitioned in such a way to have an inner disk surrounded by an outer ring[24]. Material properties at ambient temperature were assigned to the inner disk, while the rest of it was supposed to be at 90 °C. The reason for this choice are borrowed from the temperature field of the static analysis (Figure 2-25), where the highest temperature values were reached in the center.
The frequency at which the TSM mode happens in this configuration is shown in Table 3-1 along with the reference values.

Thermal Field	Frequency [*Hz*]
Uniform (@23°C)	9935576
Uniform (@90°C)	9935735
Gradient (23÷90 °C)	9937420

Table 3-1. Comparison of frequency shifts with uniform and gradient thermal fields.

It can be noted that the frequency at which the disk vibrates in the case of the temperature gradient is much higher than the two uniform temperature cases. In particular, an increase of 1.7 kHz was detected with the 90 °C uniform thermal field. In other words, the frequency shift observed in the last case is one order of magnitude higher than what expected from previous result (Figure 3-7).
Obviously, this difference must be an effect of nothing else than the temperature gradient. This is because results out the FEM analysis only are compared to each other, with no reference to the experimental values.

[24] The circular sector was split in half for meshing purposes.

Moreover, another important conclusion can be drawn by analyzing the resulting mode shape.

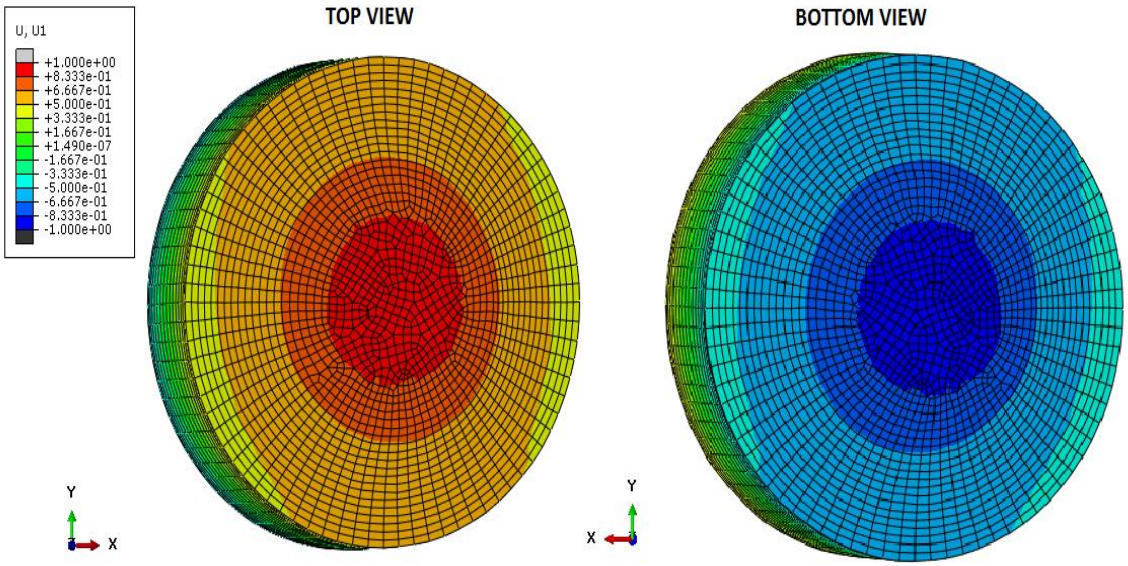

Figure 3-12. Mode shape: thermal gradient case.

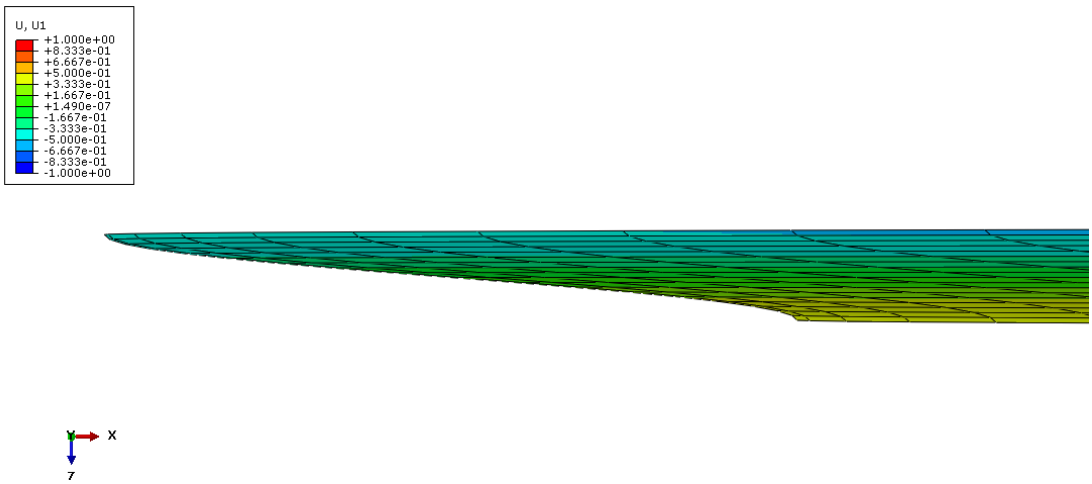

Figure 3-13. Thickness deformed shape: thermal gradient case.

It can be noted that the displacement field is not uniform as it happened for the previous case. However, it is still a TSM mode and this is confirmed by the thickness' deformed shape (Figure 3-13) and by both the values and the color-grid of Figure 3-12.

Displacements are maximum at the center. This is something expected; it can be explained by the concept of *energy trapping*, which was mentioned in the introduction (section 1.2). A higher temperature at the center of the disk implies a higher thickness in that same area. This ultimately causes the displacements to be maximum at the center.
The fact that the deformed shape can be linked to a known theoretical concept is also a confirmation of the FEM model validity.

CHAPTER 4

This last chapter deals with the concluding remarks of the thesis, highlighting the most important results as well as suggestions for further research.

4.1 Conclusions

This work has provided an overview of the effects of temperature on the innovative quartz crystal microbalance.

The device was heated by using the built-in heater circuitry. The temperature distribution was measured by means of infrared thermography. In order to do so, the microbalance's emissivity was measured at first. The major conclusion of these experiments was that the quartz disk temperature measurements exhibited regions of high uncertainty in correspondence to the heater and electrode areas characterized by very low emissivity.
A finite element model was implemented to the reproduce the experimental conditions and achieve a more reliable temperature map of the whole crystal. The model was compared with the experimental data in the areas of low uncertainty to validate its predictions. An agreement within the measurement accuracy was achieved.
However, the major conclusion of this part of the work was that a thermal gradient will appear on the quartz disk when the microbalance is heated up. More specifically, the central part of the disk will reach higher temperatures with respect to the surroundings.

Deformed shape and stresses were computed by means of the same finite element model. Results showed that the crystal deforms in a pothole shape (the central part of the disk slipped at the bottom). Additionally, the device was found to be safe in terms of mechanical resistance. However, one major question arose concerning the disk-to-supports interaction. In fact, in the present work the Von Mises stress value was found to be spurious in the areas of contact. This is because the model did not take into account the sliding of the crystal during expansion. Anyway, the performed experimental activity showed that no damages nor sliding was been detected during different thermal cycles and testing.

The microbalance's thickness shear frequency was investigated in the second part of the work. According to present literature, the effects of thermal gradients on the frequency-temperature curve have not been subject of extensive research. This is mainly because the majority of the devices are heated by a warmed enclosure leading to small gradients. Conversely, in the case under study, as discussed earlier, temperature is not uniform.

A finite element model was developed to perform dynamic analysis. It was shown that anisotropic material properties are needed to determine correctly the modal behavior of the device. Moreover, the ability of the model to deliver correct results when the crystal was at ambient temperature was proved. In fact, both the extracted eigenvalue and the mode shape associated with it were coherent with theory and experimental results.

The model was then tested to predict the microbalance's frequency-temperature curve under uniform thermal fields. Significant discrepancies were detected between model and experimental behavior. However, it was proved that these discrepancies were compatible with the uncertainty of elastic coefficients, density, CTE and angle of cut values.

An analysis, including a thermal gradient was therefore carried out. The main finding was that the frequency at which the device vibrated was much higher than what detected in case of uniform temperature distribution. This finding suggests the necessity of correcting for this shift when operating the microbalance. Clearly, due to the preliminary nature of this study, further research is needed to understand how to limit this frequency shifts and the repeatability of the phenomena.

ANNEXES

ANNEX A

```
%%--------------------
%  Code for quartz's ELASTIC TENSOR base change
%  MetroSpace LAB, 2015
%  Paolo Raddani
%%--------------------
clc
clear
close all
%--------------------
%%Rotation angle
t = degtorad(-90 + 35.25);

%%Base Rotation Matrix
U = [1 0 0; 0 cos(t) -sin(t); 0 sin(t) cos(t)];

%%Elastic coefficients matrix.
%Voigt Tensorial notation is here used.
%Reading Data from Excel file

filename = 'ElasticCoeff_Temperature.xlsx';

sheet = 1;

choice = questdlg('Which Temperature to Consider?', 'Temperature [°C]', '23', '78',
'145', '145');

switch choice

    case '23'

        C11 = xlsread(filename, sheet, 'B2');
        C12 = xlsread(filename, sheet, 'E2');
        C13 = xlsread(filename, sheet, 'F2');
        C33 = xlsread(filename, sheet, 'C2');
        C14 = xlsread(filename, sheet, 'G2');
        C44 = xlsread(filename, sheet, 'D2');
        C66 = xlsread(filename, sheet, 'H2');

    case '78'
```

```
        C11 = xlsread(filename, sheet, 'B3');
        C12 = xlsread(filename, sheet, 'E3');
        C13 = xlsread(filename, sheet, 'F3');
        C33 = xlsread(filename, sheet, 'C3');
        C14 = xlsread(filename, sheet, 'G3');
        C44 = xlsread(filename, sheet, 'D3');
        C66 = xlsread(filename, sheet, 'H3');

    case '145'

        C11 = xlsread(filename, sheet, 'B4');
        C12 = xlsread(filename, sheet, 'E4');
        C13 = xlsread(filename, sheet, 'F4');
        C33 = xlsread(filename, sheet, 'C4');
        C14 = xlsread(filename, sheet, 'G4');
        C44 = xlsread(filename, sheet, 'D4');
        C66 = xlsread(filename, sheet, 'H4');

end


C = [C11 C12 C13 C14 0 0;
    C12 C11 C13 -C14 0 0;
    C13 C13 C33 0 0 0;
    C14 -C14 0 C44 0 0;
    0 0 0 0 C44 C14;
    0 0 0 0 C14 C66];


%%Transformation matrix

T = [U(1,1)^2 U(2,1)^2 U(3,1)^2 2*U(2,1)*U(3,1) 2*U(1,1)*U(3,1) 2*U(2,1)*U(1,1);
    U(1,2)^2 U(2,2)^2 U(3,2)^2 2*U(2,2)*U(3,2) 2*U(1,2)*U(3,2) 2*U(1,2)*U(2,2);
    U(1,3)^2 U(2,3)^2 U(3,3)^2 2*U(2,3)*U(3,3) 2*U(1,3)*U(3,3) 2*U(1,3)*U(2,3);
    U(1,2)*U(1,3) U(2,2)*U(2,3) U(3,2)*U(3,3) U(2,3)*U(3,2)+U(2,2)*U(3,3)
U(1,3)*U(3,2)+U(1,2)*U(3,3) U(1,3)*U(2,2)+U(1,2)*U(2,3);
    U(1,1)*U(1,3) U(2,1)*U(2,3) U(3,1)*U(3,3) U(2,3)*U(3,1)+U(2,1)*U(3,3)
U(1,3)*U(3,1)+U(1,1)*U(3,3) U(1,3)*U(2,1)+U(2,3)*U(1,1);
    U(1,1)*U(1,2) U(2,1)*U(2,2) U(3,1)*U(3,2) U(2,2)*U(3,1)+U(3,2)*U(2,1)
U(1,2)*U(3,1)+U(3,2)*U(1,1) U(1,2)*U(2,1)+U(2,2)*U(1,1)];

%%Base Transformation
%Abaqus conventions are here introduced

disp('Elastic coefficient after base change:')
Cp = T*C*T'

%%Possible shear frequencies;
h = 0.167*10^-3;
```

```
rho = 2648.7;

f_vect = zeros(1,3);
for i=1:3

    f_vect(i) = 1/(2*h)*sqrt(Cp(i+3,i+3)*10^9/rho);

end

disp('Possible shear frequencies:')
f_vect
```

Published with MATLAB® R2014b

ANNEX B

```
%%--------------------
% CODE FOR THERMAL MAP EXTRACTION of the CRYSTAL SAMPLE
% Developed for Metro Space Lab
% Paolo RADDANI, 2015
%%--------------------
clear
close
clc
%%--------------------
%%Getting infos

display('Load video file:');
[FileName,PathName] = uigetfile({'*.mp4; *.m4v; *.mov'},'Select the video file')

cd(PathName)

video = VideoReader(FileName)

%%Define interval of temperatures

Tmax = input('Define Maximum Temperature:  ');
Tmin = input('Define Minimum Temperature:  ');

save( 'T.mat', 'Tmax','Tmin' )
%%--------------------
%%Define when to acquire the frame

time = input('When to acquire the frame [s]?:   ');

video.CurrentTime = time;

k = 1;
while video.CurrentTime <= time+0.5
    s(k).cdata = readFrame(video);
    k = k+1;
end

for i=1:k-2
    image(s(i).cdata)
    figure
end
close
```

```
n = input('Which frame to analyze?:  ');

close all
image(s(n).cdata)
frame = rgb2gray(s(n).cdata);
imsave(imshow(frame))
pause

%%------------------
%%Defining ROI and filtering

disp('Create a polygonal ROI. Double click to finish.')
[bw, xi, yi] = roipoly;

frame_filt = immultiply(bw,frame);
figure
imsave(imshow(frame_filt))
pause
s = regionprops(bw, frame_filt, {'MinIntensity','MaxIntensity','MeanIntensity'});

Tmax_framefilt = double(s.MaxIntensity)*(Tmax - Tmin)/255 + Tmin
Tmin_framefilt = double(s.MinIntensity)*(Tmax - Tmin)/255 + Tmin
Tmean_framefilt = double(s.MeanIntensity)*(Tmax - Tmin)/255 + Tmin

%%-------------------
%%Calculations for entire image

frame = double(frame)*(Tmax - Tmin)/255 + Tmin;

figure
image(frame(:,:),'CDataMapping','scaled');
axis image
colormap hot
h = colorbar;
h.Label.String = 'Temperature °C';
title('Entire Frame')
xlabel('X Pixels'); ylabel('Y Pixels');
savefig('EntireImage_Temp')

%%-------------------
%%Calculations for ROI

xmin = min(xi)-5; xmax = max(xi)+5;
ymin = min(yi)-5; ymax = max(yi)+5;

frame_filt = double(frame_filt(:,:))*(Tmax - Tmin)/255 + Tmin;  %°C
save frame_filt frame_filt -ascii
```

```
figure
image(frame_filt(:,:),'CDataMapping','scaled');
axis image
axis([xmin xmax ymin ymax])
colormap hot
h = colorbar;
h.Label.String = 'Temperature °C';
title('Selected ROI')
xlabel('X Pixels'); ylabel('Y Pixels');
savefig('ROI_Temp')
```

Published with MATLAB® R2014b

ANNEX C

```
%%--------------------
% CODE FOR EMISSIVITY MAP EXTRACTION
% Developed for Metro Space Lab
% Paolo RADDANI, 2015
%%--------------------
clc
clear
close all
%%--------------------
%%Data
%%NOTE: TEMPERATURES MUST BE EXPRESSED in K!

Tth = load('frame_filt','-ascii') + 273.15; %K

Tbk = 22.7 + 273.15; %K

Tc = 67.6 + 273.15;  %k

load('T.mat');
Tmax = Tmax + 273.15;   %K
Tmin = Tmin + 273.15;   %K

%%--------------------
%%Global calculations

epsm = (Tth.^4 - Tbk^4)/(Tc^4 - Tbk^4); %K/K

save epsm epsm -ascii

dTbk = 0.2; %Don't need to convert it to K!
dTc = 0.28;
dTth = 3/sqrt(3);

depsm = uncert_epsm(Tth, Tbk, Tc, dTth, dTbk, dTc);

%%--------------------
%%Plots

figure(1)
image(epsm(:,:),'CDataMapping','scaled')
axis image
colormap bone
cmap = colormap;
```

```
newcmap = cmap(end:-1:1,:);
colormap(newcmap)
h = colorbar;
h.Label.String = 'Emissivity';
title('GLOBAL')
xlabel('X Pixels'); ylabel('Y Pixels');
savefig('epsm')


figure(2)
image(depsm(:,:),'CDataMapping','scaled')
colormap jet
h = colorbar;
h.Label.String = 'Uncertainty';
title('GLOBAL')
xlabel('X Pixels'); ylabel('Y Pixels');

%%--------------------
%%Interactive free hand drawing

choice = questdlg('Do you want to zoom-in a region?','Zoom');

switch choice
    case 'Yes'

        disp('Please draw a region. Double click to finish.')

        figure(3)

        img = imread('frame_filt.jpg');
        h_im = imshow(img);
        e = imfreehand(gca);
        position = wait(e);
        pos = getPosition(e);
        pos(end+1,:) = pos(1,:);

        BW = createMask(e, h_im);
        close


        figure('units','normalized','outerposition',[0 0 1 1])
        subplot(221)
        image(epsm(:,:),'CDataMapping','scaled')
        hold on
        plot(pos(:,1), pos(:,2), 'k', 'LineWidth',2)
        hold off
        axis image
        colormap jet
        h = colorbar;
```

```
h.Label.String = 'Emissivity';
title('GLOBAL')
xlabel('X Pixels'); ylabel('Y Pixels');

roi_epsm = immultiply(BW, img);
roi_epsm = ( double(roi_epsm(:,:)) )*(Tmax - Tmin)/255 + Tmin;  %K

epsm = (roi_epsm.^4 - Tbk^4)/(Tc^4 - Tbk^4);

s = regionprops(BW, img, {'Extrema',...
    'MinIntensity','MaxIntensity','MeanIntensity'});


subplot(223)
image(epsm(:,:),'CDataMapping','scaled')
h = colorbar;
h.Label.String = 'Emissivity';
title('ZOOM')
xlabel('X Pixels'); ylabel('Y Pixels');
xymin = min(s.Extrema); xymax = max(s.Extrema);
xmin = xymin(1)-5; ymin = xymin(2)-5;
xmax = xymax(1)+5; ymax = xymax(2)+5;
axis([xmin xmax ymin ymax])

subplot(224)
contour(epsm,'ShowText','on')
axis([xmin xmax ymin ymax]);
title('CONTOURS of EMISSIVITY on ZOOMED REGION')
xlabel('X Pixels'); ylabel('Y Pixels');
set(gca,'YDir','reverse')
grid on

subplot(222)
image(depsm(:,:),'CDataMapping','scaled')
axis([xmin xmax ymin ymax]);
h = colorbar;
h.Label.String = 'Uncertainty';
title('ZOOM')
xlabel('X Pixels'); ylabel('Y Pixels');

%%Statistical Calculations

Tmax_epsm = ( double(s.MaxIntensity) )*(Tmax-Tmin)/255 + Tmin; %K
epsm_max = (Tmax_epsm^4 - Tbk^4)/(Tc^4 - Tbk^4)

Tmin_epsm = ( double(s.MinIntensity) )*(Tmax-Tmin)/255 + Tmin; %K
epsm_min = (Tmin_epsm^4 - Tbk^4)/(Tc^4 - Tbk^4)

Tmean_epsm = ( double(s.MeanIntensity) )*(Tmax-Tmin)/255 + Tmin; %K
```

```
        epsm_mean = (Tmean_epsm^4 - Tbk^4)/(Tc^4 - Tbk^4)

        depsm_max = uncert_epsm(Tmax_epsm,Tbk,Tc,dTth,dTbk,dTc)
        depsm_min = uncert_epsm(Tmin_epsm,Tbk,Tc,dTth,dTbk,dTc)
        depsm_mean = uncert_epsm(Tmean_epsm,Tbk,Tc,dTth,dTbk,dTc)

        rel_err = depsm_mean/epsm_mean


        %%Saving data
        load('r.mat');
        choice2 = questdlg('Do you want to store the data?','Save');

        switch choice2
            case 'Yes'
                choice3 = questdlg('Wich material are you zooming-
in?','Save','Crystal','Deposit','Heater','Heater');
                switch choice3
                    case 'Crystal'
                        xlswrite('Average_Emissivity.xlsx',epsm_mean,1,['A'
num2str(rc)])
                        xlswrite('Average_Emissivity.xlsx',depsm_mean,1,['B'
num2str(rc)])
                        rc = rc+1;
                        save('r.mat','rc','rd','rh')
                    case 'Deposit'
                        xlswrite('Average_Emissivity.xlsx',epsm_mean,1,['G'
num2str(rd)])
                        xlswrite('Average_Emissivity.xlsx',depsm_mean,1,['H'
num2str(rd)])
                        rd = rd+1;
                        save('r.mat','rc','rd','rh')
                    case 'Heater'
                        xlswrite('Average_Emissivity.xlsx',epsm_mean,1,['D'
num2str(rh)])
                        xlswrite('Average_Emissivity.xlsx',depsm_mean,1,['E'
num2str(rh)])
                        rh = rh+1;
                        save('r.mat','rc','rd','rh')
                end


            case 'No'
                return
            case 'Cancel'
                return
        end
```

```
    case 'No'
        return
    case 'Cancel'
        return
end
```

Published with MATLAB® R2014b

ANNEX D

```
%%--------------------
% CODE FOR QCM TESTING
% Developed for Metro Space Lab
% Paolo RADDANI, 2015
%%--------------------
clear
close all
clc
%%--------------------
%%Getting infos & Calculations

Tmax_test = 103 + 273.15;   %K
Tmin_test = 24 + 273.15;    %K

Tbk = 22.7 + 273.15;    %K

Tth_test = imread('frame_test.jpg');
imshow(Tth_test)
Tth_test = double(Tth_test)*( Tmax_test - Tmin_test )/255 + Tmin_test; %K


choice = questdlg('Which emissivity to consider?',...
        'Material Selection',...
        'Crystal','Heater','Deposit','Deposit');

switch choice
    case 'Crystal'
        epsm = xlsread('Average_Emissivity.xlsx',1,'L5');
        depsm = xlsread('Average_Emissivity.xlsx',1,'M5');
    case 'Heater'
        epsm = xlsread('Average_Emissivity.xlsx',1,'L8');
        depsm = xlsread('Average_Emissivity.xlsx',1,'M8');
    case 'Deposit'
        epsm = xlsread('Average_Emissivity.xlsx',1,'L11');
        depsm = xlsread('Average_Emissivity.xlsx',1,'M11');
end


%%------------------
%%Defining ROI and filtering

disp('Create a polygonal ROI. Double click to finish.')
[bw_test, xi, yi] = roipoly;
```

```
pos = [xi yi];
pos(end+1,:) = pos(1,:);

frame_filt_test = immultiply(double(bw_test),Tth_test); %K
s = regionprops(bw_test, frame_filt_test,
{'MinIntensity','MaxIntensity','MeanIntensity'});

Tmax_framefilt_test = ( ( double(s.MaxIntensity)^4 - (1 - epsm)*Tbk^4 )/epsm ).^(1/4)
-273.15
Tmin_framefilt_test = ( ( double(s.MinIntensity)^4 - (1 - epsm)*Tbk^4 )/epsm ).^(1/4)
-273.15
Tmean_framefilt_test = ( ( double(s.MeanIntensity)^4 - (1 - epsm)*Tbk^4 )/epsm
).^(1/4) -273.15

%%-------------------
%%Calculations for ROI
%%Problem: There are some 0 values in frame_filt

Tc_corr_test = ( ( Tth_test.^4 - (1 - epsm)*Tbk^4 )/epsm ).^(1/4); %K
Tc_corr_test = Tc_corr_test - 273.15; %°C

xmin = min(xi)-5; xmax = max(xi)+5;
ymin = min(yi)-5; ymax = max(yi)+5;

figure('units','normalized','outerposition',[0 0 1 1])

subplot(221)
image(imread('frame_test.jpg'),'CDataMapping','scaled')
hold on
plot(pos(:,1), pos(:,2), 'k', 'LineWidth',2)
hold off
colormap jet
title('Entire Image')
xlabel('X Pixels'); ylabel('Y Pixels');

subplot(223)
image(Tc_corr_test(:,:),'CDataMapping','scaled');
axis image
axis([xmin xmax ymin ymax])
h = colorbar;
h.Label.String = 'Temperature °C';
title('Selected ROI')
xlabel('X Pixels'); ylabel('Y Pixels');
savefig('ROI_Temp_test')

%%Uncertainty of Tc_corr

dTth = 3/sqrt(3);
dTbk = 0.20;
```

```
dTc_corr = uncert_Tc_corr(Tth_test,epsm,Tbk,dTth,depsm,dTbk);

s = regionprops(bw_test, dTc_corr, {'MinIntensity','MaxIntensity','MeanIntensity'});

dTc_corr_max = double(s.MaxIntensity);
dTc_corr_min = double(s.MinIntensity);
dTc_corr_mean = double(s.MeanIntensity)


subplot(224)
image(dTc_corr(:,:),'CDataMapping','scaled');
axis image
axis([xmin xmax ymin ymax])
h = colorbar;
h.Label.String = 'Uncertainty';
title('Selected ROI')
xlabel('X Pixels'); ylabel('Y Pixels');
```

Published with MATLAB® R2014b

ANNEX E

The isotropic material properties used in chapter two are here reported.

	QUARTZ	*Unit*
Elastic modulus	97.2	*GPa*
Poisson's ratio	0.17	-

Table 0-1. Isotropic material properties.

It is possible to compute the shear modulus by means of the theory of linear elasticity.

$$G = \frac{E}{2(1+\upsilon)} \tag{0.1}$$

where G is the shear modulus, E is the Young modulus and υ is the Poisson's ratio. Eq. 0.1 yields a shear modulus of 41.5 GPa.

If this value were introduced in Eq. 1.3, it would be concluded that the frequency of vibration should be of 11.86 MHz. The FEM confirms this result as well (Figure 0-1).

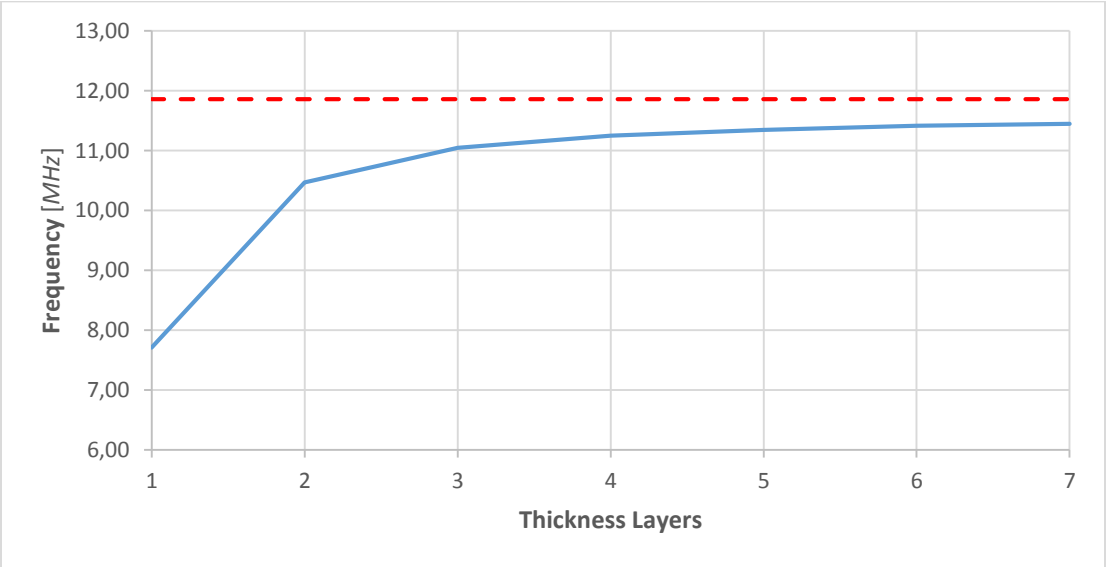

Figure 0-1. FEM result with isotropic material properties.

However, the frequency value computed with this material model is too far from reality to be accepted. As it shown in chapter three, TSM should take place at around 10 MHz.

Moreover, with such a model, two modes orthogonal to each other were found to happen at the same frequency. It was then not clear which one of the two modes would be excited when the microbalance was operated in practice.

Anyway, even if the model here presented was discarded in favor of a more accurate one, this discussion has influenced the rest of the work in two ways. First, it showed that the frequency of vibration strongly depends on how fine the mesh is in the thickness direction. Second, it made the research team aware of the necessity of introducing anisotropic material properties.

REFERENCES

IHS Global Ltd, 1978. Heat transfer by free convection and radiation – simply shaped bodies in air and other fluids. *ESDU 77031*.

Anon., 2007. CO2 capture by adsorption with nitrogen enriched carbons. *Fuel,* September, 86(14), p. 2204–2212.

Ballato, A. & Vig, J., 1978. Static and Dynamic Frequency-Temperature Behavior of Singly and Doubly Rotated, Oven-Controlled Quartz Resonators. *32nd Annual Symposium on Frequency Control,* pp. 180-188.

Barucci, M., Benner, L., Scheeres, D. J. & Giorgini, J. D., 2013. *Near-Earth Asteroid 341843 (2008 EV5) Target Of ESA'S Marcopolo-R Mission,* Mountain View, California, USA: National Radio Astronomy Observatory / SETI Institute.

Battaglia, et al., 2004. Development of a micro-balance system for dust and water vapour detection in the Mars atmosphere. *Advances in Space Research 33,* pp. 2258-2262.

Bechmann, R., Ballato, A. & Lukaszek, T. J., 1962. Higher-Order Temperature Coefficients of the Elastic Stiffinesses and Compliances of Alpha-Quartz. *Procedings of the IRE,* pp. 1812-1822.

Budyansky, M., Madormo, C., Maciaszek, J. L. & Lykotrafitis, G., 2011. Coherent gradient sensing microscopy (micro-CGS): A microscale curvature detection technique. *Optics and Lasers in Engineering,* Volume 49, pp. 874-879.

Capelle, B. et al., 1990. Mode Shape Analysis Techniques Using Synchrotron X-ray Topography. *44th Annual Symposium On Frequency Control,* pp. 416-423.

Capone, B. R., Kahan, A., Brown, R. N. & Buckmelter, J. R., 1970. Quartz Crystal Radiation Effects. *IEEE Trans. Nuclear Sci.,* Volume 17, pp. 217-221.

CCIR, 1990. *Standard Frequency and Time Signals (Study Group 7).* U.S.A, CCIR.

Cengel, Y. A. & Ghajar, A. J., 2011. *Heat and Mass Transfer: Fundamentals & Applications.* 4th ed. U.S.A.: McGraw-Hill.

Coats, A. W. & Redfern, J. P., 1963. Thermogravimetric Analysis. *Analyst,* Volume 88.

Curie & Curie, 1880. An oscillating quartz crystal mass detector. *Rendu 91,* pp. 294-297.

Cuthbertson, R. D., Stinton, H. C. & Wheeler, R. W., 1979. The Use of a Thermogravimetric Analyser for the Investigation of Particulates and Hydrocarbons in Diesel Engine Exhaust. *SAE Technical Paper 790814.*

Doebelin, E. O., 2008. Misure e incertezza di misure. In: *Strumenti e metodi di misura.* Milano: McGraw-Hill, pp. 61-98.

eFunda, 2015. *Heat Transfer: View Factors.* [Online] Available at: http://www.efunda.com [Accessed 21 July 2015].

ESA, 2012. *JUICE assessment study report (Yellow Book),* ESA: ESA/SRE(2011)18.

Filler, R. L., 1988. The Acceleration Sensitivity of Quartz Crystal Oscillators: A Review. *IEEE Transactions on Ultrasonics, Ferroelectrics, and Frequency Control,* 35(3), pp. 297-305.

Fowle, F. E., 1919. The Non-Selective Transmissibility of Radiation Through Dry and Moist Air. *Astrophysical Journal,* Volume 38, pp. 392-406.

Haruta, K. & Spencer, W. J., 1966. X-ray Diffraction Study of Vibrational Modes. *20th Annual Symposium on Frequency Control,* pp. 1-13.

Hewlett Packard, 1997. *Fundamentals of Quartz Oscillators - Application Note 200-2,* U.S.A: Hewlett Packard.

Incropera, F. P. & De Witt, D. P., 2011. *Foundamentals of Heat and Mass Transer.* 6th ed. U.S.A.: Wiley.

Kesim, Y. E., Battal, E., Tanrikulu, M. Y. & Okyay, A. K., 2014. An all-ZnO microbolometer for infrared imaging. *Infrared Physics & Technology,* Volume 67, p. 245–249.

Klokholm, E., 1969. An Apparatus for Measuring Stress in Thin Films. *The Review of Scientific Instruments,* 40(8), pp. 1054-1058.

Kolahdouz, M., Östling, M. & Radamson, H., 2012. High performance infra-red detectors based on Si/SiGe multilayers quantum structure. *Materials Science and Engineering: B,* 177(17), pp. 1563-1566.

Kosinski, J. A., Gualtieri, J. G. & Ballato, A., 1992. Thermoelastic Coefficients of Alpha Quartz. *IEE Transactions on ultrasonic, ferroelectrics and frequency control,* 34(4), pp. 502-507.

Kulkarni, A. K., 1997. Electrical and structural characteristics of chromium thin films deposited on glass and alumina substrates. *Thin Solid Films,* Volume 301, pp. 17-22.

Kusters, J. A., 1985. Resonator and Device Technology. *Precision Frequency Control,* Volume I, pp. 161-183.

Kusters, J. A. & Vig, J. R., 1989. Thermal Hysteresis in Quartz Resonators - A Review. *44th Annual Symposium on Frequency Control,* pp. 165-175.

Lippmann, G., 1881. Principe de la conservation de l'électricité. *Annales de chimie et de physique 24,* p. 145.

Longobardo, A., Palomba, E., Dirri, F. & Scaccabarozzi, D., 2015. *BB Test report: TN 4300,* Milan: Politecnico di Milano.

Lu, C.-s., 1974. Mass determination with piezoelectric quartz crystal resonators. *Journal of Vacuum Science Technology 12,* pp. 578-583.

Mamleev, V. & Bourbigot, S., 2005. Modulated thermogravimetry in analysis of decomposition kinetics. *Chemical Engineering Science,* 60(III), p. 747–766.

Martin, S., Senturia, S., Frye, G. & Ricco, A., 1993. Effect of Surface Roughness on the Response of Thickness-Shear Mode Resonators in Liquids. *Analytical Chemistry 65,* pp. 2910-2922.

McKeown, D., 1998. Quartz crystal instrumentation for space research. *SPIE's International Symposium on Optical Science, Engineering and Instrumentation,* pp. 113-125.

Meeker, T. R. & Vig, J. R., 1991. The Aging of Bulk Acoustic Wave Resonators, Oscillators and Filters. *45th Annual Symposium on Frequency Control.*

O'Sullivan, C. & Guilbault, G., 1999. Commercial quartz crystal microbalances – theory and applications. *Biosensors & Bioelectronics 14,* p. 663–670.

Ohno, I., 1995. Temperature variations of the elastic properties of alfa-quartz up to the alpha-beta transition. *J. Phys. Earth,* Volume 43, pp. 157-169.

Paesler, M. A. & Fritzsche, H., 1974. Measurement of internal stress in thin films. *The Review of Scientific Instruments,* 45(1), pp. 1114-1115.

Palomba, E. et al., 2012. VISTA: a thermogravimetry/biosensor system for in-situ analysis of planetary surfaces. *9th International Planetary Probe Workshop.*

Repas, R., 2008. *Sensor Sense: Piezoelectric Force Sensors.* [Online] Available at: http://machinedesign.com [Accessed 15 07 2015].

Santos, M. F., Fujiwara, E., de Paula, F. D. & Suzuki, C. K., 2013. Opacity measurements on quartz and its influence on silica glass properties. *International Journal of Mineral Processing,* Volume 124, pp. 141-144.

Sauerbrey, G., 1959. Verwendung von Schwingquarzen zur Wägung dünner Schichten und zur Mikrowägung. *Zeitschrift für Physik 155 (2),* pp. 206-222.

Scaccabarozzi, D., Saggin, B. & Palomba, E., 2014. *CAM Thermo-Mechanical Design Report TN 4500,* Milan: Politecnico di Milano.

Srama, Kempf & Moragas-Klostermeyer, 2011. The cosmic dust analyser onboard cassini: ten years of discoveries. *CEAS Space J. 2,* pp. 3-16.

Taylor, J. R., 1997. Propagation of uncertainties. In: *An introduction to error analysis.* Sausalito, California: University Science Books , pp. 45-79.

Tiersten, H., 1969. *Linear Piezoelectric Plate Vibrations.* New York: Plenum.

Valentin, J. P., Théobald, G. & Gagnepain, J. J., 1984. Frequency shifts arising from in-plane temperature gradient distribution in quartz resonators. *38th Annual Frequency Control Symposium,* pp. 157-163.

Vannucci, 2008. Anisotropia: analisi e metodi di rappresentazione. In: *Materiali Compositi.* Pisa: DIS, p. 173.

Vig, J. R., 2004. *QUARTZ CRYSTAL RESONATORS AND OSCILLATORS For Frequency Control and Timing Applications - A TUTORIAL,* Fort Monmouth, NJ, USA: US Army Communications-Electronics Research, Development & Engineering Center.

Vig, J. R. & Walls, F. L., 1994. Fundamental Limits on the Frequency Instabilities of Quartz Crystal Oscillators. *IEEE Int'l Frequency Control Symposium,* pp. 506-523.

Ward, W. R., 1992. The Constants of Alpha Quartz. *14th Piezoelectric Devices Conference and Exhibition,* pp. 1-15.

Wu, D. H., Tsai, Y. J. & Yen, Y. T., 2003. Robust design of quartz crystal microbalance using finite element and Taguchi method. *Sensors and Actuators B,* Volume 92, p. 337–344.

Wudy, F., Stock, C. & Gores, H. J., 2009. Electrochemical: quartz microbalance. In: *Measurements Method.* Regensburg: Elsevier, pp. 660-672.